


Activity-induced phase transition in a quantum many-body systemKyosuke Adachi ^{1,2}, Kazuaki Takasan ^{3,4} and Kyogo Kawaguchi ^{1,5,6}¹*Nonequilibrium Physics of Living Matter RIKEN Hakubi Research Team, RIKEN Center for Biosystems Dynamics Research, 2-2-3 Minatojima-minamimachi, Chuo-ku, Kobe 650-0047, Japan*²*RIKEN Interdisciplinary Theoretical and Mathematical Sciences Program, 2-1 Hirosawa, Wako 351-0198, Japan*³*Department of Physics, University of California, Berkeley, California 94720, USA*⁴*Materials Sciences Division, Lawrence Berkeley National Laboratory, Berkeley, California 94720, USA*⁵*RIKEN Cluster for Pioneering Research, 2-2-3 Minatojima-minamimachi, Chuo-ku, Kobe 650-0047, Japan*⁶*Universal Biology Institute, The University of Tokyo, Bunkyo-ku, Tokyo 113-0033, Japan*

(Received 15 July 2021; accepted 15 February 2022; published 11 March 2022)

A crowd of nonequilibrium entities can show phase transition behaviors that are prohibited in conventional equilibrium setups. An interesting question is whether similar activity-driven phase transitions also occur in pure quantum systems. Here we investigate a classical anisotropic lattice gas model that undergoes motility-induced phase separation and extend the model to the quantum regime. The resulting model is a quantum many-body model that undergoes quantum phase transitions induced by non-Hermiticity. The quantum phase diagram includes active phase transitions involving phase separation, microphase separation, and flocking. The quantum phase transitions are identified as the transitions of dynamical paths in the classical kinetics upon the application of biasing fields. Our approach sheds light on the useful connection between classical nonequilibrium kinetics and non-Hermitian quantum physics.

DOI: [10.1103/PhysRevResearch.4.013194](https://doi.org/10.1103/PhysRevResearch.4.013194)**I. INTRODUCTION**

The collective dynamics of active or self-driven components can lead to phase transitions and pattern formations that are prohibited in equilibrium systems [1]. Recent works have shown the properties of materials such as surface flow [2], odd responses [3], and anomalous topological defect dynamics [4,5] that can be realized by introducing activity into the design. In addition to the application in biophysical examples [6], combining the understandings of active systems with a broader range of models in condensed matter should bring progress not only in nonequilibrium physics but also in material science [7].

Although the scope of active matter has greatly widened in the past years [8], its quantum analog has so far not been explicitly proposed. Past works have pointed out how similar equations of time evolution may appear between classical active matter and models from other regions of physics; the Toner-Tu type equation [9] describing the dynamics of microwave-driven 2D electron liquid [10], high effective temperature realized at the interface between two 3D systems with a difference in chemical potential [11,12], and a self-propelled particle expressed by a spinor with spin-orbit coupling [13], to name a few. However, activity-induced phase transitions in the spirit of the Vicsek model, i.e., spontaneous symmetry

breaking induced in a many-body model by nonequilibrium driving, are yet to be identified in a quantum setup.

In recent years, advances in atomic-molecular-optical experiments have allowed precise control over open quantum systems [14–17], encouraging the exploration of nonequilibrium physics in various courses including topological phases [18–25] and quantum critical phenomena [26–29] in non-Hermitian setups. In light of these developments, it is now sensible to consider how the quantum versions of classical nonequilibrium processes can be realized, and ask whether there exist new phases of matter induced by activity in quantum many-body systems.

One of the simplest models of phase transition in active matter is the exclusion process with uniaxial activity [30]. In this model, the particles undergo exclusive random walk with uniaxially biased hopping depending on their internal degree of freedom. This model undergoes anisotropic phase separation upon increasing the strength of biased-hopping (i.e., self-driven motility), which could be thought of as an example of motility-induced phase separation (MIPS) [31]. MIPS has been observed in Brownian particle [32] and lattice [33] simulations as well as in experiments involving artificial [34] and biological [35] materials. Although the basic mechanism of MIPS is seemingly simple (i.e., accumulation of particles at high-density regions due to the slowing down of self-propelled motion), the components that cause the phase separation behavior [36,37] and the critical properties of the phase transitions [38–41] are still under active discussion, and may depend on the details of the model [42–44].

Similar models with uniaxial biased motion have been considered as the driven lattice gas, where phase behaviors

Published by the American Physical Society under the terms of the Creative Commons Attribution 4.0 International license. Further distribution of this work must maintain attribution to the author(s) and the published article's title, journal citation, and DOI.

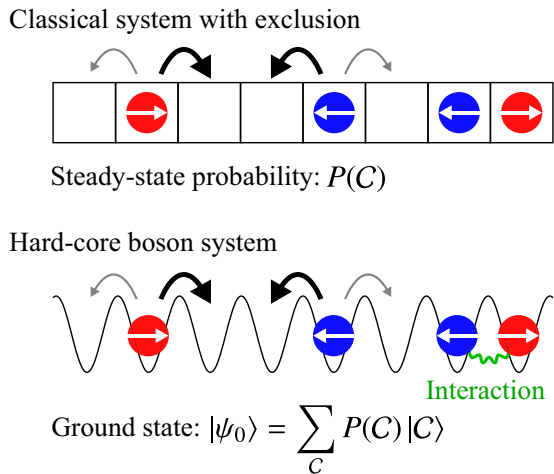


FIG. 1. Correspondence between a classical model of active matter and a quantum model of hard-core bosons. In the classical model, particles stochastically move with asymmetric hopping rates. In the quantum model, hard-core bosons asymmetrically hop due to the non-Hermitian terms in the Hamiltonian, and also feel nearest-neighbor interactions additional to the hard-core repulsion. $|C\rangle$ is the Fock basis corresponding to the configuration of the particles C .

and spatiotemporal correlations have been shown to drastically change due to the anisotropy [45–48]. Anisotropic models of active lattice gas have also appeared in the context of flocking [49,50], where a macroscopic number of particles collectively move in one direction [51]. Yet, despite the simplicity of these models, the relation between the activity-induced phase transitions and the anomalous behaviors owing to the spatial anisotropy has not been extensively discussed.

In this work, we introduce a quantum many-body model on a lattice with an analog of uniaxial activity. First, we show that this minimally simple model embeds a classical interacting particle model within its parameter space, where the self-driving property of the particles is encoded in the non-Hermiticity of the Hamiltonian. We find that the embedded classical model undergoes anisotropic MIPS with interesting properties even in the seemingly trivial homogeneous phase; long-range correlation that has a characteristic singularity in the structure factor. Outside of the classical model, the activity-induced phase transitions appear as the property of the ground state of the quantum many-body model. By investigating the quantum phase diagram via Monte Carlo (MC) simulations, we find that the model exhibits flocking and microphase-separated phases that do not appear in the embedded classical model, and further show the relation of these phases to the dynamical phases. Finally, we remark on the possibility of implementing the model in an ultracold atomic gas experiment. This work demonstrates how activity-induced phase transitions, so far exclusively studied in classical models, can occur also as quantum phase transitions.

II. NON-HERMITIAN HARD-CORE BOSONS AND CLASSICAL ACTIVE LATTICE GAS

The model we study here (Fig. 1) involves quantum hard-core bosons with “spin” s ($= \pm 1$) in a $L_x \times L_y$ rectangular

lattice with periodic boundary condition (PBC):

$$\begin{aligned}
 H(J, \varepsilon, U_1, U_2, h) = & -J \sum_{(i,j),s} (a_{i,s}^\dagger a_{j,s} + a_{j,s}^\dagger a_{i,s}) \\
 & - \varepsilon J \sum_{i,s} s (a_{i,s}^\dagger a_{i-\hat{x},s} - a_{i,s}^\dagger a_{i+\hat{x},s}) - h \sum_{i,s} a_{i,s}^\dagger a_{i,-s} \\
 & - U_1 \sum_{(i,j)} \hat{n}_i \hat{n}_j - U_2 \sum_i \hat{m}_i (\hat{n}_{i+\hat{x}} - \hat{n}_{i-\hat{x}}) + (4J + h)N,
 \end{aligned} \tag{1}$$

where $\hat{n}_{i,s} := a_{i,s}^\dagger a_{i,s}$ is the local density of particles with spin s , $\hat{n}_i := \hat{n}_{i,+} + \hat{n}_{i,-}$, and $\hat{m}_i := \hat{n}_{i,+} - \hat{n}_{i,-}$. \hat{x} is the unit horizontal translation, and N is the fixed total number of particles. The second term in (1) describes the spin-dependent asymmetric hopping ($J > 0$ and $-1 \leq \varepsilon \leq 1$), which is non-Hermitian for $\varepsilon \neq 0$. The fourth and fifth terms represent the spin-independent and dependent nearest-neighbor interactions, respectively, with their general form discussed in Appendix D 1. The U_2 term represents a nearest-neighbor coupling between the local magnetization \hat{m}_i and the density gradient $\hat{n}_{i+\hat{x}} - \hat{n}_{i-\hat{x}}$, which favors positive (negative) magnetization at the left (right) boundary of a cluster of particles for $U_2 > 0$ [see typical configurations in Fig. 6(b)]. The U_2 term is necessary to connect the quantum Hamiltonian (1) to the classical stochastic model (see Appendix A), although the precise form is likely not important in observing the activity-induced phase transition. We take $h > 0$ and consider a partial Fock space where multiple particles cannot occupy a single site regardless of their spins.

The physical interpretation of a non-Hermitian quantum system is ambiguous due to the complex energy spectrum. For the case of (1), however, its eigenvalue with the smallest real part is unique and real (which we call E_0), and the corresponding eigenstate can be taken to have all its elements real and positive (which we denote as $|\psi_0\rangle$). This is due to the Perron-Frobenius theorem, which can be applied since the off-diagonal elements of H in the Fock representation are all real and nonpositive. We can also show that E_0 is bounded below (see Appendix D 3). In this work, we focus on how the ground state $|\psi_0\rangle$ (with the ground-state energy E_0) changes according to the change of parameters in H . Throughout this paper, we set $\hbar = 1$, so that energy has the dimension of the inverse of time.

III. ANISOTROPIC ACTIVE LATTICE GAS

Within the parameter space of (1), there is a special subspace defined by $U_1 = 2J$ and $U_2 = \varepsilon J$, where the Hamiltonian can be mapped [52,53] to the transition rate matrix of an active lattice gas model (ALG) (see Appendix A). The ALG here is an N -particle model where the particles are exclusively hopping within the $L_x \times L_y$ rectangular lattice with the PBC [Fig. 2(a)]. Each particle has a spin s ($= \pm 1$) as its internal variable, which sets the rate of asymmetric hopping in the x direction as $(1 + \varepsilon s)J$ and $(1 - \varepsilon s)J$ for the positive and negative directions, respectively. The y -directional hopping rate is J , the spin flipping rate is h , and we define the density as $\rho := N/(L_x L_y)$ ($0 < \rho < 1$).

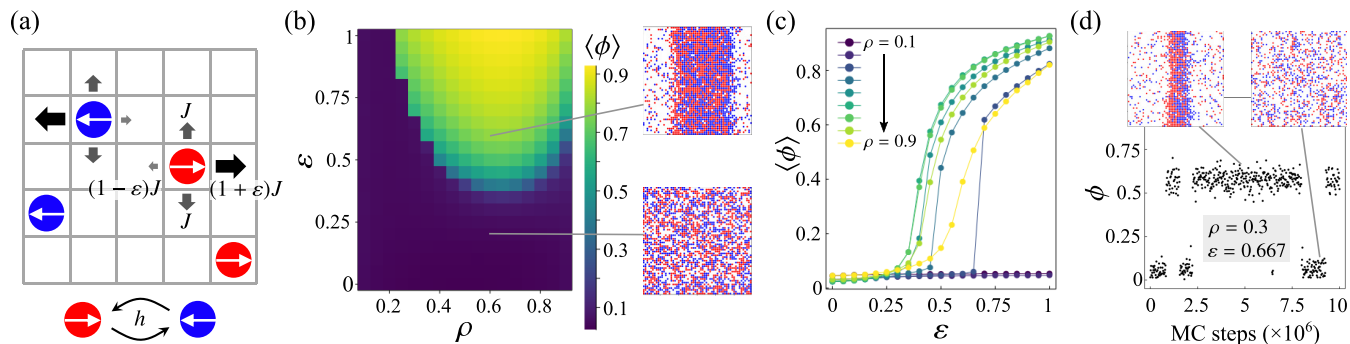


FIG. 2. (a) Anisotropic ALG. Each particle with spin hops to the nearest-neighbor site with the spin-dependent rate or flips its spin with the rate h . (b) Heatmap of the steady-state order parameter $\langle \phi \rangle$ in the $\rho - \varepsilon$ plane. Typical configurations of the PS and homogeneous states are also shown. (c) ε dependence of $\langle \phi \rangle$ for different values of ρ , which is another plot of (b). (d) Time dependence of ϕ at a discontinuous transition point ($\rho = 0.3$ and $\varepsilon = 0.667$) with typical snapshots of bistable PS and homogeneous states. For (b), (c), and (d), we set $L_x = L_y = 60$.

Before considering the full quantum model (1), we characterize the static and dynamical properties of the ALG as a model of anisotropic active matter. In the following, we set $h = 0.025J$ in MC simulations (see Appendix B 1). As we increase ε , the ALG shows a phase transition from the homogeneous state to the phase-separated (PS) state [see the typical configurations in Fig. 2(b)], where the particles moving in the $+x$ or $-x$ direction are blocked by others moving in the opposite direction. Similar types of phase transitions have been discussed in two-species driven lattice gas models [54–57] and recently regarded as a MIPS transition in an ALG [30]. We define the order parameter for the PS state as $\langle \phi \rangle := \langle |\sum_j \exp(-2\pi i x_j/L_x) n(\mathbf{r}_j)| \sin(\pi/L_x)/[\sin(\pi\rho)L_y] \rangle$ [58,59], where $\mathbf{r}_j := (x_j, y_j)$ and $n(\mathbf{r}_j)$ are the spatial coordinate and occupancy of the site j , respectively, $\langle \dots \rangle$ is the ensemble average in the steady state, and $\langle \phi \rangle = 1$ for the fully PS state. For $L_x = L_y = 60$, we obtain the $\rho - \varepsilon$ phase diagram as a heatmap of $\langle \phi \rangle$ [Fig. 2(b)]. The ε dependence of $\langle \phi \rangle$ [Fig. 2(c)] and the bistability at the transition point [Fig. 2(d)] suggest that the transition is discontinuous for low density ($\rho \lesssim 0.4$), as observed in similar models [57], though further investigation is needed to clarify whether the transition is still discontinuous in the thermodynamic limit. On the other hand, $\langle \phi \rangle$ is a continuous function of ε in the density region with $\rho \gtrsim 0.4$ [Fig. 2(c)].

A. Long-range correlation in the homogeneous state

According to the studies on driven lattice gas models and coarse-grained Langevin models [45,47,48], long-range density correlation is generically believed to appear in the nonequilibrium steady state with spatial anisotropy of dynamics. To examine whether the ALG shows long-range density correlation in the homogeneous steady state, we calculate the structure factor $S(\mathbf{k}) := \sum_j \exp(-i\mathbf{k} \cdot \mathbf{r}_j) C(\mathbf{r}_j)$, where $C(\mathbf{r}) := (L_x L_y)^{-1} \sum_i \langle [n(\mathbf{r}_i + \mathbf{r}) - \rho][n(\mathbf{r}_i) - \rho] \rangle$ is the correlation function that should be short-ranged in the equilibrium limit ($\varepsilon \rightarrow 0$). As illustrated in Fig. 3(a) and colored dots in Fig. 3(c) for $L_x = L_y = 200$, $\rho = 0.6$, and $\varepsilon = 0.2$, we find a singularity of $S(\mathbf{k})$ at $\mathbf{k} = \mathbf{0}$, i.e., $S(k_x \rightarrow 0, k_y = 0) > S(k_x = 0, k_y \rightarrow 0)$, which means that the long-range density correlation exists as in driven lattice gas models [45].

To understand the singularity of $S(\mathbf{k})$, we apply the path-integral method [60–63] and derive the Langevin equation for the spin-density field $\rho_s(\mathbf{r}, t)$ (see Appendix B 2):

$$\partial_t \rho_s = J(\nabla^2 \rho_s - \rho_{-s} \nabla^2 \rho_s + \rho_s \nabla^2 \rho_{-s}) - 2s\varepsilon J \partial_x [(1 - \rho_+ - \rho_-) \rho_s] - h(\rho_s - \rho_{-s}) + \xi_s, \quad (2)$$

where the lattice constant is set to unity, $\langle \xi_s(\mathbf{r}, t) \rangle = 0$, and $\langle \xi_s(\mathbf{r}, t) \xi_{s'}(\mathbf{r}', t') \rangle = \delta(t - t') M_{s,s'} \delta(\mathbf{r} - \mathbf{r}')$ with a differential operator $M_{s,s'} := \delta_{s,s'} [-2J \nabla \cdot (1 - \rho_+ - \rho_-) \rho_s \nabla] + (2\delta_{s,s'} - 1)h(\rho_+ + \rho_-)$. Linearizing Eq. (2) [64–66] and adiabatically eliminating the fast variable $\rho_+(\mathbf{r}, t) - \rho_-(\mathbf{r}, t)$, we obtain the linear Langevin equation for the density fluctuation $\varphi(\mathbf{r}, t) := \rho_+(\mathbf{r}, t) + \rho_-(\mathbf{r}, t) - \rho$, which can be solved in the Fourier space using $\varphi(\mathbf{k}, t) := \int d^2\mathbf{r} \exp(-i\mathbf{k} \cdot \mathbf{r}) \varphi(\mathbf{r}, t)$ (see Appendix B 3). Under these approximations, we can calculate the structure factor $S_{\text{lin}}(\mathbf{k}) := (L_x L_y)^{-1} \lim_{t \rightarrow \infty} \langle |\varphi(\mathbf{k}, t)|^2 \rangle$,

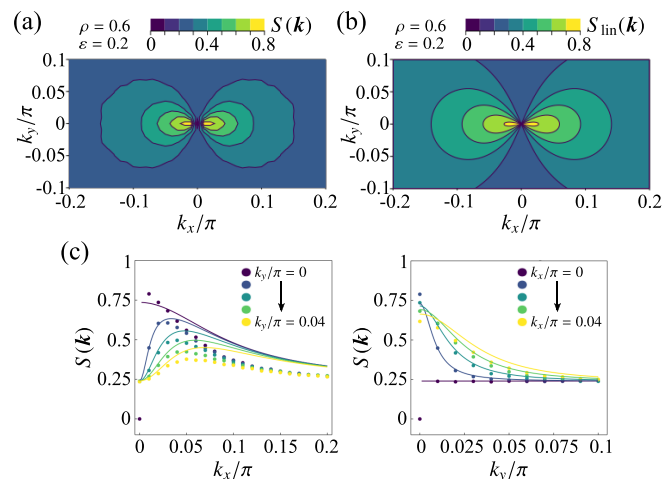


FIG. 3. (a) Contour plot of the structure factor $S(\mathbf{k})$ obtained numerically at $\rho = 0.6$ and $\varepsilon = 0.2$ (homogeneous state). (b) Contour plot of the linearized structure factor $S_{\text{lin}}(\mathbf{k})$ [Eq. (3)] for the same parameters as (a). (c) Quantitative comparison between $S(\mathbf{k})$ (dots) and $S_{\text{lin}}(\mathbf{k})$ (lines) for the same parameters as (a). Note $S(\mathbf{k} = \mathbf{0}) = 0$ due to the particle number conservation. For (a) and (c), we used $L_x = L_y = 200$.

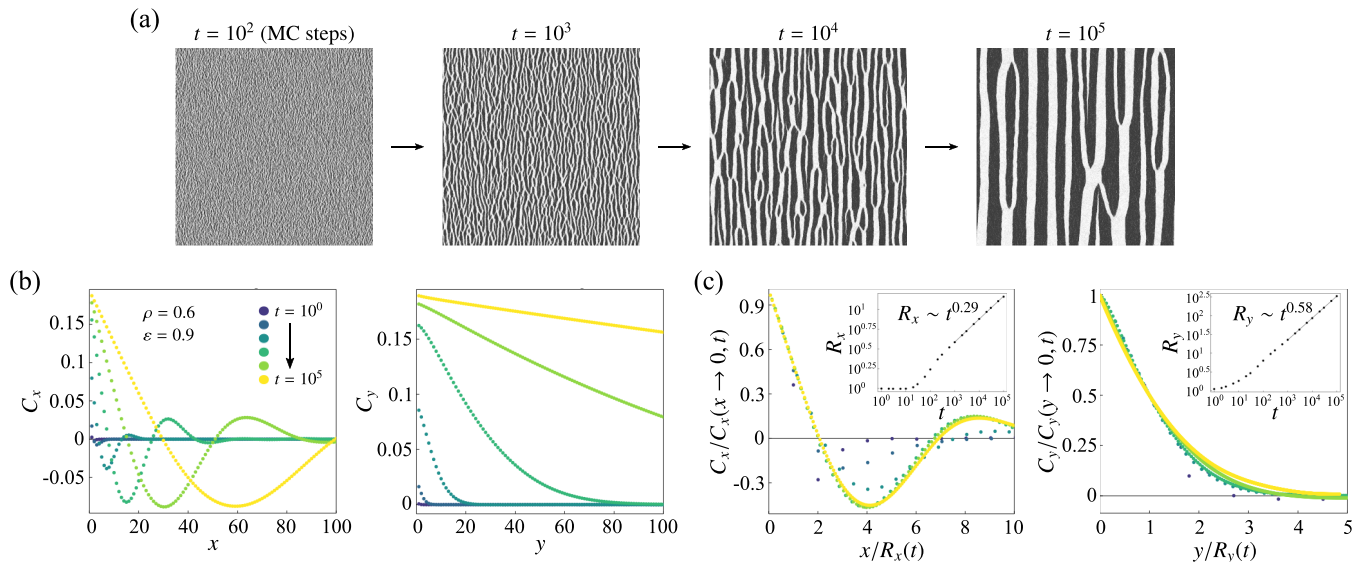


FIG. 4. (a) Coarsening process toward phase separation. Each snapshot is a quarter square of the original system with $L_x = L_y = 3200$. (b) Space and time dependence of the density correlation functions along the x axis (C_x) and the y axis (C_y). (c) Rescaled correlation functions as functions of the rescaled coordinates. Time evolution of the domain sizes $R_x(t)$ and $R_y(t)$ is shown in the inset, where the fitted line for the well-scaled region (10^3 MC steps $\leq t \leq 10^5$ MC steps) is also shown. For all figures, we set $\rho = 0.6$ and $\varepsilon = 0.9$.

leading to

$$S_{\text{lin}}(\mathbf{k}) = (1 - \rho)\rho \times \frac{[2h + J(1 - \rho)\mathbf{k}^2]\mathbf{k}^2 + 4\varepsilon^2 J(1 - \rho)k_x^2}{[2h + J(1 - \rho)\mathbf{k}^2]\mathbf{k}^2 - 4\varepsilon^2 J(1 - \rho)(2\rho - 1)k_x^2}. \quad (3)$$

As shown in Fig. 3(b) and colored lines in Fig. 3(c), $S_{\text{lin}}(\mathbf{k})$ captures the qualitative feature observed in the simulation. In particular, the singularity at $\mathbf{k} = \mathbf{0}$ is quantified [47] by $S_{\text{lin}}(k_x \rightarrow 0, k_y = 0)/S_{\text{lin}}(k_x = 0, k_y \rightarrow 0) - 1 = 4\varepsilon^2 J\rho(1 - \rho)/[h - 2\varepsilon^2 J(1 - \rho)(2\rho - 1)]$, which is nonzero if $\varepsilon \neq 0$. Thus the spatial anisotropy associated with the detailed balance violation in the ALG leads to the long-range density correlation.

B. Dynamic scaling in the phase-separated state

We next investigate how the anisotropy appears in the dynamics of the PS state by focusing on the coarsening process toward phase separation [Fig. 4(a)]. We introduce $C_x(x, t) := C(x, y = 0, t)$ and $C_y(y, t) := C(x = 0, y, t)$, where $C(\mathbf{r}, t)$ is the time-dependent density correlation function. Defining the typical domain size $R_x(t)$ along the x axis as $C_x(R_x(t), t) = C_x(x \rightarrow 0, t)/2$ and $R_y(t)$ in a similar way [67], we examine the rescaled correlation function $C_x(x, t)/C_x(x \rightarrow 0, t)$ as a function of $x/R_x(t)$ and the counterpart for $C_y(y, t)$.

For $L_x = L_y = 3200$, $\rho = 0.6$, and $\varepsilon = 0.9$, we find a good scaling behavior for $10^3 \lesssim t \lesssim 10^5$, where time t is measured in units of 1 MC step [Figs. 4(b) and 4(c)]. Moreover, in the same time range, the growth dynamics shows an anisotropic power law as $R_x(t) \sim t^{\alpha_x}$ and $R_y(t) \sim t^{\alpha_y}$ with $\alpha_x < \alpha_y$ [insets in Fig. 4(c)]. Such anisotropic growth law with $\alpha_x < \alpha_y$ holds for different values of ρ or ε (see Appendix B 4).

C. Critical point properties

Recent simulations [39,40] and theories [39] of the MIPS transition have suggested that the *isotropic* MIPS critical point seems to show the Ising universality, i.e., the universality for equilibrium phase separation. In contrast, the effects of spatial anisotropy that we have described both in the homogeneous and PS states suggest that the universality of the *anisotropic* MIPS critical point in the ALG is different from the Ising universality. Furthermore, it is in fact still unclear whether the critical point of the *isotropic* MIPS generically belongs to the Ising universality class [38,41], since the macroscopic MIPS may be replaced by the microphase separation, or the bubbly phase separation [42,43], as observed in large-scale simulations [44]. In our ALG, we did not find the anisotropic counterpart of the bubbly phase separation even in simulations of relatively large systems: $(L_x, L_y) = (1200, 400)$ (see Appendix B 4).

According to the studies on anisotropic nonequilibrium systems in two dimensions [45], there may exist two different exponents related to the divergence of the correlation length at criticality, ν_x and ν_y . Based on Eq. (2), we find that the effective model which should describe the critical dynamics of the ALG coincides with that of the two-temperature lattice gas model (see Appendix B 5), in which case the exponents satisfy $\nu_y/\nu_x \simeq 2$ [68–71].

To numerically estimate the critical exponents β , ν_x , and ν_y for the ALG, we assume $\nu_y/\nu_x = 2$ and use the anisotropic finite-size scaling analysis [58,59]. Briefly, we consider the scaling hypothesis as $\langle \phi^n \rangle = L_x^{-n\beta/\nu_x} F_n(L_x^{1/\nu_x}(\varepsilon - \varepsilon_c), S)$, where F_n is a scaling function, ε_c is the critical point, and $S := L_y/L_x^{\nu_y/\nu_x} = L_y/L_x^2$. We take $S = 1/15^2$ with varying L_x . We set $\rho = 0.6$ as a rough estimate of the bottom point of the binodal curve based on Figs. 2(b) and 2(c). The results below did not qualitatively change when we took $\rho = 0.65$ (see Appendix B 6).

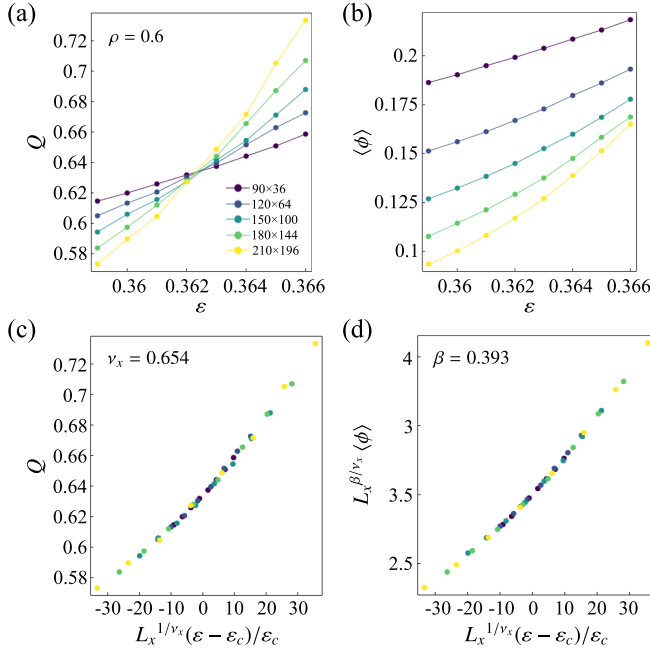


FIG. 5. (a) ε dependence of the Binder ratio Q for $\rho = 0.6$ and different system sizes with fixed $L_y/L_x^2 = 1/15^2$. The solid lines are guides for the eyes. (b) ε dependence of $\langle \phi \rangle$ for the same parameters as (a). (c) Q as a function of the rescaled ε with the best-fitted ε_c ($\simeq 0.362$) and ν_x ($\simeq 0.654$). (d) Rescaled $\langle \phi \rangle$ as a function of the rescaled ε with the best-fitted β ($\simeq 0.393$) and the same values of ε_c and ν_x as (c).

We find that the Binder ratio $Q(\varepsilon, L_x) := \langle \phi^2 \rangle^2 / \langle \phi^4 \rangle$ shows a crossing point [Fig. 5(a)], which is consistent with the scaling hypothesis. Fitting $Q(\varepsilon, L_x)$ with second-order polynomials (see Appendix B 6), we obtain $\varepsilon_c \simeq 0.36238(4)$ and $\nu_x \simeq 0.65(1)$, where the value in the bracket is the fitting error on the last significant figure. Then, fitting $\langle \phi \rangle(\varepsilon, L_x)$ [Fig. 5(b)] in a similar way, we find $\beta \simeq 0.3928(8)$. By rescaling, we confirm that Q and $\langle \phi \rangle$ respect the scaling function, consistent with the scaling hypothesis [Figs. 5(c) and 5(d)]. Note that slight changes of ν_x and β (e.g., $\nu_x = 0.6$ and $\beta = 0.35$) still give consistent scaling results for the system sizes used here (see Appendix B 6). The obtained values of ν_x and β are comparable to those of the two-temperature lattice gas model [$\nu_x \simeq 0.62(3)$ and $\beta \simeq 0.33(2)$] [71] and two-loop renormalization group calculation of the corresponding effective Langevin model ($\nu_x \simeq 0.626$ and $\beta \simeq 0.315$) [68,69,71]. Therefore our ALG model shows consistent results with the two-temperature lattice gas model within the tested regime.

IV. QUANTUM PHASE DIAGRAM AND DYNAMICAL PHASE TRANSITION

From the viewpoint of the full quantum model, the classical condition ($U_1 = 2J$ and $U_2 = \varepsilon J$) induces $E_0 = 0$. The corresponding right eigenstate $|\psi_0\rangle$ is equivalent to the steady-state distribution of the ALG (Fig. 1), and the left eigenstate is the coherent state, $\langle \psi'_0 | = \langle P | := \langle 0 | \exp(\sum_{i,s} a_{i,s})$. For the case of $\varepsilon = 0$ and $U_2 = 0$, H is Hermitian and equivalent to the ferromagnetic XXZ model with fixed magnetization [72]

(see Appendix D 2), where a first-order transition between the superfluid and phase-separated states occurs at the Heisenberg point ($U_1 = 2J$) [73]. The Heisenberg point is also special in that the right and left ground states are both coherent states.

To explore how the tendency toward MIPS comes into play beyond the classical condition, we conducted the diffusion Monte Carlo (DMC) simulation [74]. We chose horizontally elongated systems (e.g., 50×5) to reveal the typical configurations of the quantum states (see the insets in Fig. 6) within the numerically limited system size. In short, we run the Monte Carlo simulation for the ALG but with the additional steps of resampling the states based on the calculated weights of the paths. This works since the Hamiltonian can be divided into two parts $H = -W - D$, where $W := -H(J, \varepsilon, U_1 = 2J, U_2 = \varepsilon J, h)$ corresponds to the classical dynamics and D , being a diagonal matrix, can be interpreted as the resampling weights (see Appendix C).

To discuss the quantum phases, we focus on physical quantities $A(\{\hat{n}_{i,s}\})$ which are functions of the configuration of the particles and calculate $\langle A \rangle_C := \langle P | A(\{\hat{n}_{i,s}\}) | \psi_0 \rangle / \langle P | \psi_0 \rangle$. PS states are characterized by

$$\phi_{\text{PS}} := (L_x L_y)^{-1} \sum_{(i,j)} \langle (\hat{n}_i - \rho)(\hat{n}_j - \rho) \rangle_C. \quad (4)$$

For microphase-separated (mPS) states, in which the number of clusters is $O(L_x)$ [see the upper configuration in Fig. 6(b)], we utilize ϕ_{mPS} as the order parameter, which is the density of clusters with oppositely polarized edges:

$$\phi_{\text{mPS}} := L_x^{-1} \sum_{i=1}^{L_x} \langle \hat{m}_i^X (\hat{n}_{i+1}^X - \hat{n}_{i-1}^X) \rangle_C, \quad (5)$$

where $\hat{n}_i^X := L_y^{-1} \sum_{j=1}^{L_y} \hat{n}_{i\hat{x}+j\hat{y}}$ and $\hat{m}_i^X := L_y^{-1} \sum_{j=1}^{L_y} \hat{m}_{i\hat{x}+j\hat{y}}$. In the large-size limit ($L_x, L_y \rightarrow \infty$), $\phi_{\text{PS}} > 0$ and $\phi_{\text{mPS}} = 0$ for the PS state, while $\phi_{\text{PS}} > 0$ and $|\phi_{\text{mPS}}| > 0$ for the mPS state.

A. Quantum phase transitions

We first find that there is a discontinuous phase transition induced by slightly increasing U_1 from $2J$. As shown in Fig. 6(a), ϕ_{PS} increases rapidly as a function of U_1 at around $U_1 = 2J$ for a broad range of ε ($= 0, 0.2, 0.6$) and $U_2 = \varepsilon J$, with the ground-state energy E_0 having a kink at $U_1 = 2J$. This line of phase separation transition extends from the first-order transition in the XXZ model ($\varepsilon = 0$) [72,73]. Second, for high enough ε ($= 0.6$), a drop in ϕ_{PS} and an increase in ϕ_{mPS} occur simultaneously as U_2 crosses εJ [Fig. 6(b)]. As also indicated from the typical configuration and the kink in E_0 [Fig. 6(b)], this is expected to be a discontinuous transition between the PS and mPS states. For low ε ($= 0, 0.2$), in contrast, we do not see this transition [Fig. 6(b)]. We observed similar transitions in a one-dimensional (1D) setup, even though the corresponding classical model does not show MIPS (see Appendix D 6).

Next, we consider increasing ε while fixing $U_1 = 2J$ and $U_2 = 0$. Intriguingly, we find that a ferromagnetic order appears without phase separation for high ε ($\gtrsim 0.4$), indicated by $M^2 := N^{-2} \langle (\sum_i \hat{m}_i)^2 \rangle_C$ [Fig. 7(a)]. Such polar order, which should be accompanied by flow due to the asymmetric

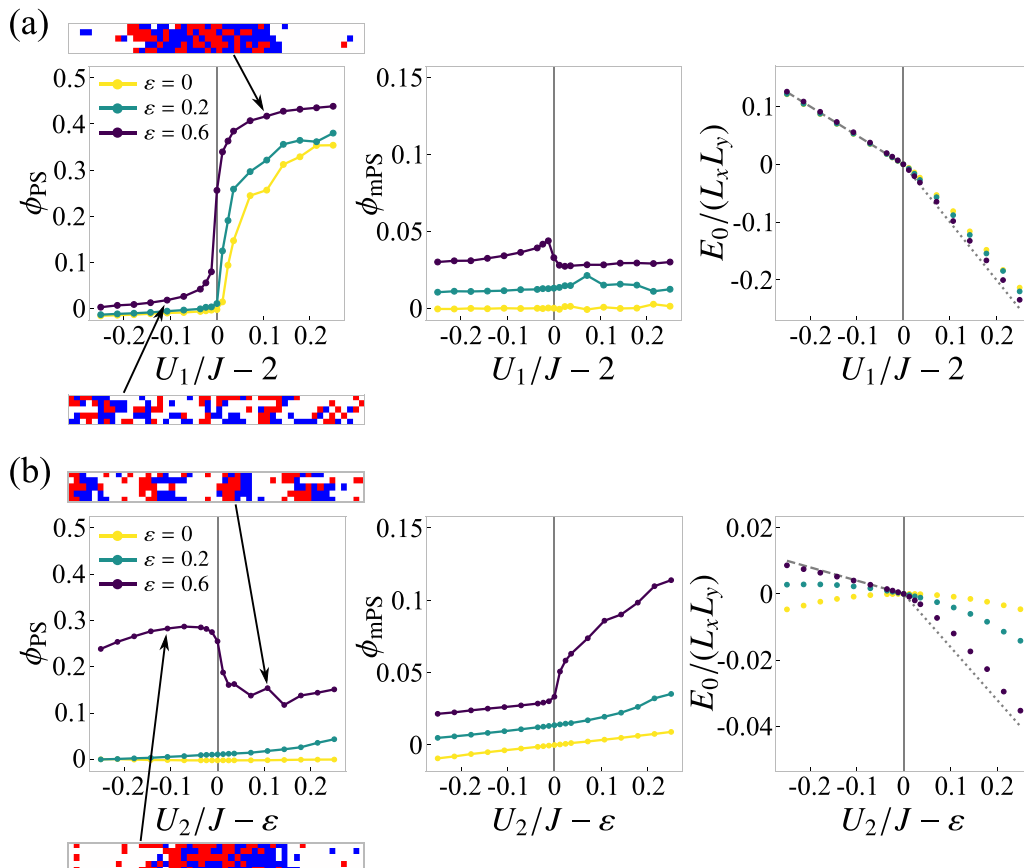


FIG. 6. (a) U_1 dependence with $U_2 = \varepsilon J$ and (b) U_2 dependence with $U_1 = 2J$ of the order parameters (ϕ_{PS} and ϕ_{mPS}) and the ground-state energy (E_0) for $\rho = 0.5$, $h = 0.025J$, and $\varepsilon = 0, 0.2, 0.6$ in 50×5 systems with typical configurations. In the figures of E_0 , we also plotted the analytical results of $\langle H \rangle_C$ for (a) a disordered state (dashed) and a PS state (dotted) or (b) a mPS state with one (dashed) or four (dotted) clusters (see Appendix D 4).

hopping, is reminiscent of the flocking of self-propelled particles observed, e.g., in the Vicsek model [75], although our model (1) does not include explicit polar interactions. We stress that the mPS and polar states observed in the quantum model are not stable in the embedded classical model in any parameter region [see Fig. 2(b) for the phase diagram of the classical model].

To investigate whether the polar order remains in larger systems, we further performed simulations in 1D systems. The size dependence of M^2 and ϕ_{PS} in 1D systems [Fig. 7(b)] shows that the polar state is destabilized and instead the PS

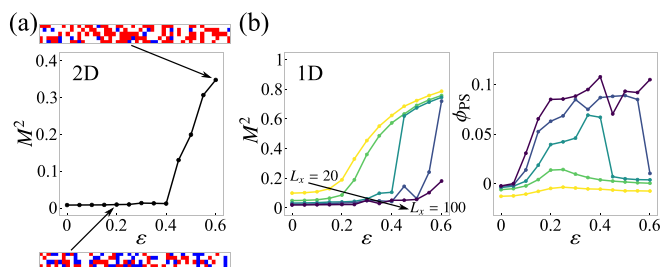


FIG. 7. (a) ε dependence of the squared magnetization M^2 and typical configurations in 50×5 systems. (b) ε dependence of M^2 and ϕ_{PS} in 1D systems with $L_x = 20, 40, 60, 80$, and 100 . In both (a) and (b), we set $\rho = 0.5$, $h = 0.025J$, $U_1 = 2J$, and $U_2 = 0$.

state appears as the system size becomes larger. In addition, the discontinuous changes in M^2 and ϕ_{PS} indicate the bistability of the polar and PS states in finite systems. Similarly, in large two-dimensional systems, the PS state can replace the polar state, as observed in the U_2 dependence of M^2 and ϕ_{PS} for the system with size 50×5 (see Appendix D 5). Therefore we find that the non-Hermitian asymmetric hopping terms alone (with $U_2 = 0$) will lead to either the polar state or the PS state, which are the quantum analogs of the flocking and MIPS states, respectively.

In Fig. 8, we show the phase diagram for a system with size 30×3 . First, Fig. 8(a) is the $U_2 - \varepsilon$ phase diagram around the classical line ($U_1 = 2J$ and $U_2 = \varepsilon J$) indicated in red. In addition to the classical MIPS, the PS-mPS transition occurs when crossing the classical line at high ε [see Fig. 6(b)]. Next, Figs. 8(b) and 8(c) display the $U_1 - U_2$ phase diagrams around the classical line. For low ε ($= 0.2$) [Fig. 8(b)], we find that the U_1 -induced phase separation transition [Fig. 6(a)] occurs robustly against U_2 -perturbation from the classical line. In contrast, for high ε ($= 0.6$) [Fig. 8(c)], slight changes in U_1 and U_2 around the classical line can lead to the mPS and polar states.

The full phase diagram is difficult to explore since the DMC simulation becomes less reliable when deviations of the parameters from the classical line ($U_1 - 2J$ and $U_2 - \varepsilon J$) are large [see the approximation in Eq. (C2)].

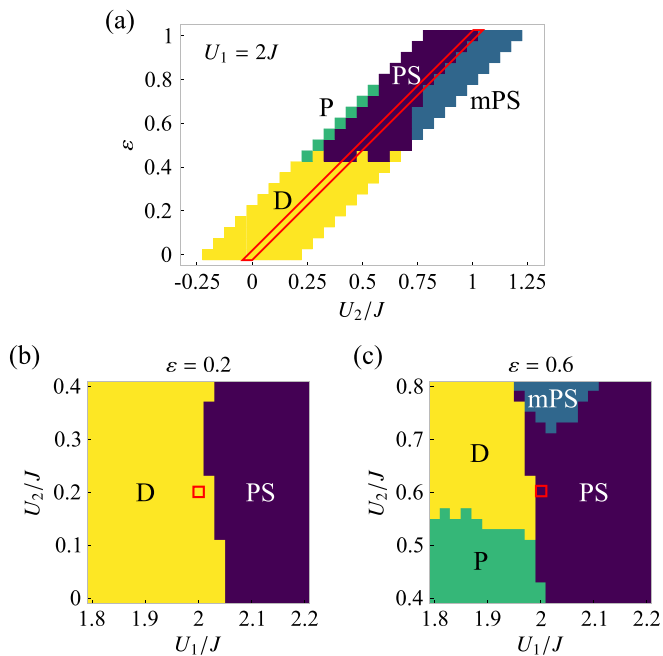


FIG. 8. Ground-state phase diagrams of the quantum model. (a) U_2 - ε phase diagram for $U_1 = 2J$ around the classical line (red box), with PS ($\phi_{PS} > 0.1$ and $\phi_{mPS} \leq 0.1$), mPS ($\phi_{mPS} > 0.1$), P (polar, $M^2 > 0.1$), and D (disordered, otherwise) states. $U_1 - U_2$ phase diagrams for (b) $\varepsilon = 0.2$ and (c) $\varepsilon = 0.6$ around the cross section of the classical line (red box). In all figures, we set $\rho = 0.5$ and $h = 0.025J$.

Nevertheless, there are symmetries in this system that indicate the positions of the phase boundaries in a wider parameter region (Fig. 9). First, we have $E_0(J, -\varepsilon, U_1, -U_2, h) = E_0(J, \varepsilon, U_1, U_2, h)$ which is due to $H(J, \varepsilon, U_1, U_2, h) = \hat{U}^\dagger H(J, -\varepsilon, U_1, -U_2, h) \hat{U}$, where \hat{U} is the unitary operator of spin reversal. We also have $E_0(J, -\varepsilon, U_1, U_2, h) = E_0(J, \varepsilon, U_1, U_2, h)$ since $H(J, -\varepsilon, U_1, U_2, h)^\dagger = H(J, \varepsilon, U_1, U_2, h)$. Since the analytical property of E_0 indicates the positions of the phase boundaries, we expect that the boundaries calculated in Fig. 8 may have corresponding phase boundaries in $\varepsilon < 0$ and/or $U_2 < 0$ regions. For example, there should be a transition for large enough $|\varepsilon|$ in crossing the dual classical line defined by $U_1 = 2J$ and $U_2 = -\varepsilon J$, which is where $E_0 = 0$ and $|\psi_0\rangle = |P\rangle$ (Fig. 9).

B. Connection to dynamical phase transition in classical kinetics

The scheme of the DMC implies an interesting connection between the quantum model and the classical kinetics. For the ALG with the transition rate matrix W , we denote the configuration of the particles at time t as $C_t = \{n_{i,s}(t)\}$, and its stochastic trajectory as $C_t = C_k$ ($t_k \leq t < t_{k+1}$) with t_k being the time point of the k th jump. For a path-dependent quantity $\bar{B}_\tau := \int_0^\tau dt B_{C_t, C_t} + \sum_k B_{C_k, C_{k+1}}$ defined using an arbitrary real matrix B that acts on the Fock space, we introduce

$$\lambda^W(B) := \lim_{\tau \rightarrow \infty} \frac{1}{\tau} \ln \langle \exp(\bar{B}_\tau) \rangle^W, \quad (6)$$

where the ensemble average $\langle \dots \rangle^W$ is taken over the trajectories in the ALG. $\lambda^W(B)$ is equivalent to the dominant

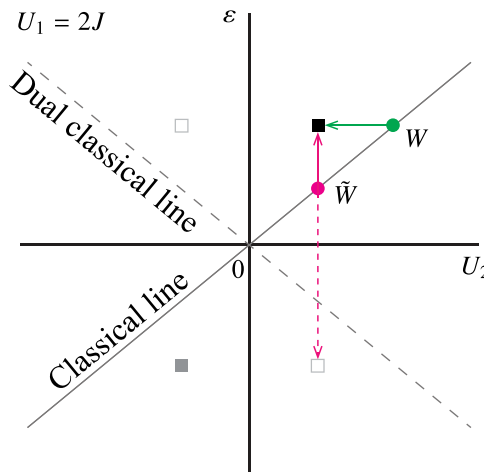


FIG. 9. Schematic of the U_2 - ε plane at $U_1 = 2J$. The Hamiltonian has two symmetries (see the main text), meaning that the points indicated by squares all have the same value of E_0 . The classical line ($U_2 = \varepsilon J$) and the dual classical line ($U_2 = -\varepsilon J$) have $E_0 = 0$. The same Hamiltonian (e.g., black square) can be described in multiple ways of classical stochastic dynamics (e.g., W and \tilde{W}) with bias (e.g., green and magenta arrows).

eigenvalue of a biased transition rate matrix [76,77]:

$$W_{C,C'}^B := (1 - \delta_{C,C'}) W_{C,C'} e^{B_{C,C'}} + \delta_{C,C'} (W_{C,C'} + B_{C,C'}). \quad (7)$$

Typical paths that appear in the biased dynamics can become dramatically different from the original dynamics, which is the hallmark of dynamical phase transition that can be captured by the (non)analytical behavior of $\lambda^W(B)$ [77]. Biased kinetics and dynamical phase transition have been studied with interests in exploring glassy systems and in characterizing phases in models of active matter [78–80].

The quantum Hamiltonian (1) can be interpreted as the transition rate matrix with bias by writing $H = -W^B$, where the bias is $B = u_1 F + u_2 G$ with $F_{C,C'} := \langle C | \sum_{(i,j)} \hat{n}_i \hat{n}_j | C' \rangle$ and $G_{C,C'} := \langle C | \sum_i \hat{m}_i (\hat{n}_{i+\hat{x}} - \hat{n}_{i-\hat{x}}) | C' \rangle$ being diagonal matrices. Here, $|C\rangle$ is the Fock basis corresponding to the configuration C , and $u_1 := U_1 - 2J$ and $u_2 := U_2 - \varepsilon J$ quantify the displacement from the classical line. We then arrive at

$$E_0(J, \varepsilon, U_1, U_2, h) = -\lambda^W(u_1 F + u_2 G), \quad (8)$$

which means that the quantum phase transitions, captured by the property of E_0 , are equivalent to the dynamical phase transitions induced by the bias $u_1 F + u_2 G$. The bias here has a clear interpretation: increasing u_1 and u_2 favors larger ϕ_{PS} and ϕ_{mPS} , respectively.

More generally, we may consider an arbitrary pair of a transition rate matrix \tilde{W} and bias \tilde{B} that satisfies $H = -\tilde{W}^{\tilde{B}}$. One interesting choice is $\tilde{W} = -H(J = U_1/2, \varepsilon = 2U_2/U_1, U_1, U_2, h)$, which is a matrix with the same diagonal elements as $-H$ but with the off-diagonal elements tuned so that $\sum_C \tilde{W}_{C,C'} = 0$. The corresponding bias will be

$$\tilde{B}_{C,C'} = |V_{C,C'}| \ln \frac{J}{J_0} + \ln \frac{1 + \varepsilon V_{C,C'}}{1 + \varepsilon_0 V_{C,C'}}, \quad (9)$$

which is nondiagonal and non-Hermitian (Fig. 9). Here, V is a skew-Hermitian matrix given by

$$V_{C,C'} = \sum_{i,s} s \langle C | (a_{i,s}^\dagger a_{i-\hat{x},s} - a_{i,s}^\dagger a_{i+\hat{x},s}) | C' \rangle \quad (10)$$

Introducing the entropy production by its commonly used definition [76]:

$$\sigma_{C,C'}(W') := \ln \frac{W'_{C,C'}}{W'_{C',C}}, \quad (11)$$

we find

$$\tilde{B} - \tilde{B}^\dagger = \sigma(\tilde{W}^{\tilde{B}}) - \sigma(\tilde{W}), \quad (12)$$

which indicates that the difference of entropy production defined in the biased and unbiased kinetics is exactly the non-Hermiticity of the bias \tilde{B} . We also note that there is a fluctuation theorem-like relation [76]:

$$\lambda^{\tilde{W}}(\tilde{B}) = \lambda^{\tilde{W}}(\tilde{B}^\dagger - \sigma(\tilde{W})), \quad (13)$$

which follows from $(\tilde{W}^{\tilde{B}})^\dagger = \tilde{W}^{-\sigma(\tilde{W})+\tilde{B}^\dagger}$. This symmetry, which is nothing but the $E_0(J, -\varepsilon, U_1, U_2, h) = E_0(J, \varepsilon, U_1, U_2, h)$ symmetry, is depicted as magenta arrows in Fig. 9.

We have observed the discontinuous transitions in crossing the classical line for $\rho = 0.5$ (Fig. 6), while the order parameter continuously changes through the MIPS transition along the classical line for the same ρ [Fig. 2(c)]. Similarly, models of glasses [77,81] and active matter [79] which do not undergo discontinuous transitions within the unbiased models (i.e., along the classical line in our setup) can undergo discontinuous dynamical phase transitions. Furthermore, the ε -dependent transition toward the flocking phase (Fig. 7) can be understood as the consequence of biasing the kinetics toward larger \tilde{B} , which encourages more spin-dependent asymmetric hopping and therefore dissipation. Consistent with this, dynamical phase transition induced by biasing toward higher dissipation has been reported in the studies of active Brownian particles [78–80].

V. RELEVANCE TO EXPERIMENTS

In ultracold atom experiments, the Bose-Hubbard model has already been simulated, including the quantum gas microscope which allows the measurement of the spatial configuration of the quantum states [16,82,83]. We here remark on several challenges that lie ahead in order to observe the activity-induced phase transitions using such settings.

A. Quantum experiments and preparation of the ground state

Although the non-Hermitian terms are difficult to implement in general, the asymmetric hopping terms can be realized by introducing a coherent coupling between the original square lattice and a dissipative auxiliary lattice, as proposed in Ref. [21] (Fig. 10). Such an open system is described by the quantum master equation, which can be shown to reduce to a non-Hermitian quantum mechanical system by post-selected quantum trajectories [15,21,84–86]. The direction of the asymmetric hopping can be controlled by the direction

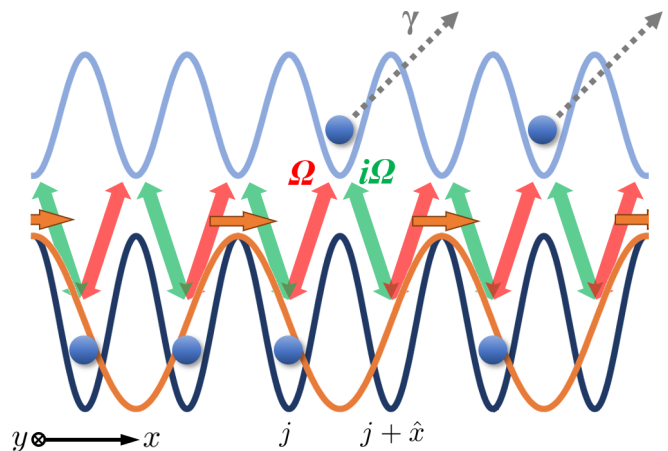


FIG. 10. Experimental implementation of the asymmetric hopping in cold atomic systems. The original optical lattice (dark blue), the dissipative optical lattice (light blue), the coherent coupling between two lattices (red and green arrows) and the running wave in the x direction (orange line) are introduced and bosonic atoms (blue balls) are loaded in the optical lattices.

of the running wave as in Fig. 10, and the spin-dependent asymmetric hopping in Eq. (1) should in principle be possible by spin-selective optical lattices [83].

Implementing nearest-neighbor interactions is also challenging for optical lattice settings, although there are various proposals such as the use of optical cavity [87], Rydberg states [88], dipolar interaction [89], and Floquet engineering [90] to overcome the difficulty.

In our model, the nearest neighbor terms do not need to be fine-tuned in order to observe the activity-induced phase transitions. For example, the DMC simulation in a 1D system [Fig. 7(b)] suggests that phase separation or polar order can be induced upon increasing ε even when U_2 is fixed at zero. The results of exact diagonalization of a small system imply that ε -induced phase transitions can also occur for $U_1 = U_2 = 0$ (Figs. 11 and 25).

Another nontrivial step in experiment is to prepare the ground state $|\psi_0\rangle$, the eigenstate with the smallest real part of the energy eigenvalue. This state is not necessarily realized at low temperature in a non-Hermitian system since the state with the largest imaginary part of the energy eigenvalue will dominate in the long-time limit. A workaround to this problem is the adiabatic preparation, as has been proposed in Refs. [26,91], for example. The idea will be to first prepare the Hermitian system ($\varepsilon = 0$) and realize the low-temperature state in a closed quantum system. The dissipation is then introduced adiabatically, i.e., turn on the asymmetric hopping term very slowly. This protocol is applicable to our setup since the Perron-Frobenius theorem guarantees the uniqueness and the realness of the ground state energy, meaning that the energy gap $\Delta = |E_1 - E_0|$ should remain nonzero in a finite system through this process at least for a finite time. Although the adiabatic theorem is invalid in the strict sense, it has been shown that, when there is a finite gap Δ , the state keeps sitting on the same state for a finite time under varying the parameters slowly [92].

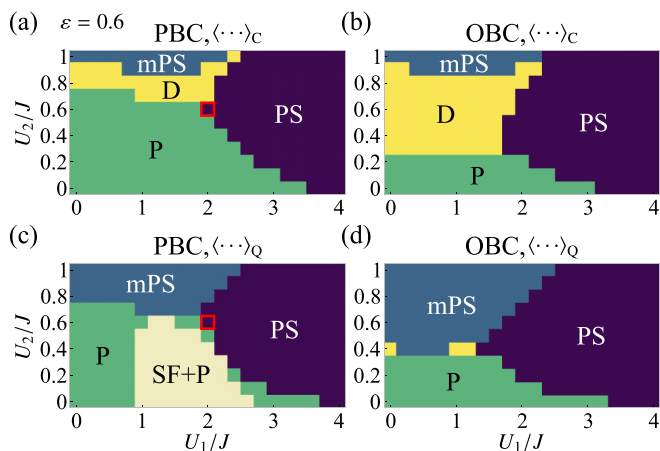


FIG. 11. U_1 - U_2 phase diagrams for $\varepsilon = 0.6$ in small 1D systems ($L_x = 12$), with PS ($\phi_{\text{PS}} > 0.05$ and $\phi_{\text{mPS}} \leq 0.3$), mPS ($\phi_{\text{mPS}} > 0.3$), P ($M^2 > 0.2$), SF (superfluid, $\phi_{\text{SF}} > 0.2$), and D (otherwise) states. The order parameters are calculated by exact diagonalization, using $\langle \cdots \rangle_C$ [(a) and (b)] or $\langle \cdots \rangle_Q$ [(c) and (d)], for the PBC [(a) and (c)] or OBC [(b) and (d)]. Superfluid states cannot be identified in DMC calculations or by using $\langle \cdots \rangle_C$ (see the main text and Appendix E). In all figures, we set $\rho = 0.5$ and $h = 0.025J$.

B. Measurable quantities and their relation to the results from the Monte Carlo simulation

The measurable quantity in open quantum systems is $\langle \cdots \rangle_Q := \langle \psi_0 | \cdots | \psi_0 \rangle$ rather than $\langle \cdots \rangle_C$ [15,84–86]. Furthermore, typical cold atom experiments are in open boundary condition (OBC) [83], in which case the exact mapping to a classical system does not exist (see Appendix D 1). To address these points, we conducted exact diagonalization for a small 1D system to check how redefining the order parameters using $\langle \cdots \rangle_Q$ and the different boundary conditions will change the result. For each of $\langle \cdots \rangle_Q$ and $\langle \cdots \rangle_C$, we define the order parameters, ϕ_{PS} , ϕ_{mPS} , and M^2 . For $\langle \cdots \rangle_Q$, we also define the order parameter for the superfluid (SF) state, which is characterized by the off-diagonal long-range correlation, as $\phi_{\text{SF}} := L_x^{-1} \sum_s \sum_{|i-j|=L_x/2} \langle a_{i,s}^\dagger a_{j,s} \rangle_Q$. Note that ϕ_{SF} for $\langle \cdots \rangle_C$ is meaningless since the SF order and the density order are equivalent ($\langle a_{i,s}^\dagger a_{j,s} \rangle_C = \langle \hat{n}_{i,s} \hat{n}_{j,s} \rangle_C$).

As shown in the phase diagram (Fig. 11), we found that all of the phases exist in the various setups, with an additional polar-SF phase which can only be captured by an off-diagonal order parameter, indicating that experiments with small systems can already lead to interesting results. The phase diagrams for other parameters with both PBC and OBC are given in Fig. 25 (Appendix E), where we quantify another choice of the expectation value $\langle \cdots \rangle_{\text{LR}} := \langle \psi'_0 | \cdots | \psi'_0 \rangle$ with $\langle \psi'_0 |$ being the left ground state [91]. All the phase diagrams are qualitatively similar, indicating that our results do not depend strongly on the choice of the expectation values and the boundary conditions.

VI. DISCUSSION

Here we have shown that a quantum many-body system can undergo activity-induced phase transition in a similar manner as in the classical MIPS but with a richer phase di-

agram. The fact that the addition of a simple spin-dependent hopping can lead to nontrivial phases indicates the potential of open quantum systems. Models with asymmetric hopping have been studied extensively in the recent context of non-Hermitian topological phases [21,93]. It will be interesting to consider the topological characterization of phases in strongly interacting systems such as in the model studied here.

In the model we have introduced, we have considered the contributions from both the deviation from equilibrium (Hermitian) and the classical condition within the same framework. This approach should be useful in importing insights from nonequilibrium classical theory to quantum many-body physics. Specifically, the correspondence between the quantum Hamiltonian and the classical transition rate matrix with bias indicates that dynamical phase transitions in general classical kinetics can in principle be probed by zero-temperature phase transitions in quantum experiments. This connection is so far restricted to a stoquastic Hamiltonian (i.e., matrix with all its off-diagonal terms being real and nonpositive); exploring other models of quantum active matter, especially nonstoquastic models that have no classical analogs, will be an interesting next step.

ACKNOWLEDGMENTS

We thank Shin-ichi Sasa, Masato Itami, Hiroyoshi Nakano, Tomohiro Soejima, Masaya Nakagawa, Yuto Ashida, Hosho Katsura, and Daiki Nishiguchi for the scientific discussions. We are also thankful to Zongping Gong, Takahiro Nemoto, Takaki Yamamoto, and Yoshihiro Michishita for helpful comments. The numerical calculations have been performed on cluster computers at RIKEN iTHEMS. K.A. is supported by JSPS KAKENHI Grant No. JP20K14435, and the Interdisciplinary Theoretical and Mathematical Sciences Program (iTHEMS) at RIKEN. K.T. is supported by the U.S. Department of Energy (DOE), Office of Science, Basic Energy Sciences (BES), under Contract No. AC02-05CH11231 within the Ultrafast Materials Science Program (KC2203). K.T. also thanks JSPS for support from Overseas Research Fellowship. K.K. is supported by JSPS KAKENHI Grants No. JP18H04760, JP18K13515, JP19H05275, and JP19H05795.

APPENDIX A: MAPPING TO THE CLASSICAL MODEL

We will show that the Hamiltonian (1) is mapped to the active lattice gas model (ALG) under the classical condition ($U_1 = 2J$ and $U_2 = \varepsilon J$). First, defining $W := -H(U_1 = 2J, U_2 = \varepsilon J)$, we can obtain

$$\begin{aligned}
 W = \hat{P} \left\{ & J \sum_{(i,j),s} (a_{i,s}^\dagger a_{j,s} + a_{j,s}^\dagger a_{i,s}) \right. \\
 & + \varepsilon J \sum_{i,s} s (a_{i,s}^\dagger a_{i-\hat{x},s} - a_{i,s}^\dagger a_{i+\hat{x},s}) \\
 & + h \sum_{i,s} a_{i,s}^\dagger a_{i,-s} - J \sum_{(i,j),s} [\hat{n}_{i,s}(1 - \hat{n}_j) + \hat{n}_{j,s}(1 - \hat{n}_i)] \\
 & \left. - \varepsilon J \sum_{i,s} s [\hat{n}_{i,s}(1 - \hat{n}_{i+\hat{x}}) - \hat{n}_{i,s}(1 - \hat{n}_{i-\hat{x}})] - h \sum_{i,s} \hat{n}_{i,s} \right\} \hat{P}. \quad (\text{A1})
 \end{aligned}$$

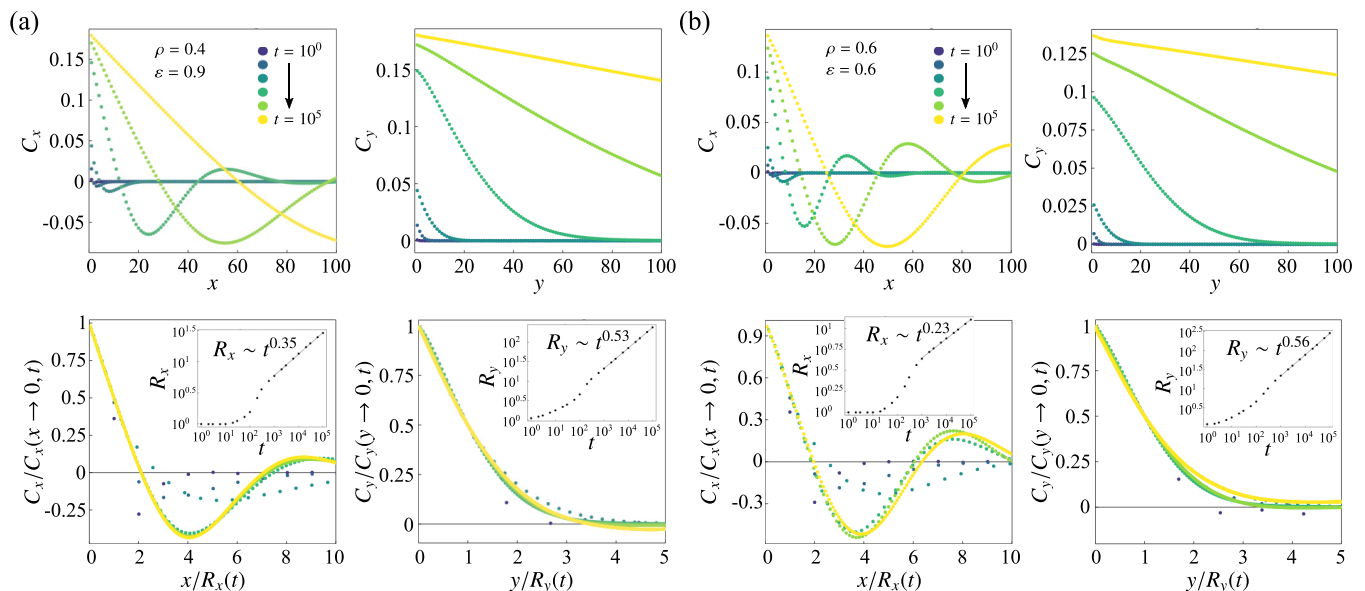


FIG. 12. (a) Space and time dependence of the density correlation functions C_x and C_y (upper figures) and their rescaled plots (lower figures) with the time dependence of the typical domain sizes R_x and R_y , for $\rho = 0.4$ and $\varepsilon = 0.9$. (b) Similar plots to (a) for $\rho = 0.6$ and $\varepsilon = 0.6$. For all figures, we set $L_x = L_y = 3200$. See Figs. 4(b) and 4(c) for $\rho = 0.6$ and $\varepsilon = 0.9$.

Here, we explicitly introduce the projection operator \hat{P} to a partial Fock space where the total particle number is N with no multiple occupancy.

Using $W_{C,C'} := \langle C|W|C' \rangle$, where $|C\rangle$ is the Fock basis corresponding to a N -particle configuration C ($:= \{n_{i,s}\}$), we can show that (i) $\sum_C W_{C,C'} = 0$ and (ii) $W_{C,C'} \geq 0$ for $C \neq C'$. Thus we can think of $W_{C,C'}$ as a transition rate matrix of a classical Markov process which yields the master equation:

$$\frac{dP(C,t)}{dt} = \sum_{C'} W_{C,C'} P(C',t), \quad (\text{A2})$$

where $P(C,t)$ is the probability of configuration C at time t . The first three terms of (A1) (nondiagonal elements of $W_{C,C'}$) represent the symmetric hopping rate, spin-dependent change in the hopping rate, and the spin flipping rate; the last three terms of (A1) (diagonal elements of $W_{C,C'}$) represent the corresponding escape rates.

Using a state vector $|\psi(t)\rangle = \sum_C P(C,t) |C\rangle$ according to the Doi-Peliti method [52,53], we can find that (A2) is nothing but the imaginary-time Schrödinger equation, $d|\psi(t)\rangle/dt = -H(U_1 = 2J, U_2 = \varepsilon J) |\psi(t)\rangle$. Thus the steady state of the ALG represented by $|\psi(t \rightarrow \infty)\rangle$ is equivalent to the ground state of the Hamiltonian, $|\psi_0\rangle$. Also, using the coherent state $\langle P| = \langle 0| \exp(\sum_{i,s} a_{i,s})$, we can express the expectation value of a classical physical quantity $A(\{n_{i,s}\})$ as $\langle A \rangle(t) = \sum_C A(C) P(C,t) = \langle P|A(\{\hat{n}_{i,s}\})|\psi(t)\rangle$. Especially for the steady state ($t \rightarrow \infty$), we obtain $\langle A \rangle(t \rightarrow \infty) = \langle P|A(\{\hat{n}_{i,s}\})|\psi_0\rangle = \langle A \rangle_C$.

APPENDIX B: DETAILS OF ANALYTICAL AND NUMERICAL RESULTS FOR ALG

1. Monte Carlo simulation

Setting a time step Δt [$= O(N^{-1})$], we first randomly choose a particle from N particles. Then, we flip the particle's

spin from s to $-s$ with probability $hN\Delta t$ or move the particle to a neighboring empty site with probability $s(1 + \varepsilon)JN\Delta t$, $s(1 - \varepsilon)JN\Delta t$, or $JN\Delta t$ depending on the hopping direction. We repeat this procedure M ($:= mN$) times, which we call m MC steps, until the total time T ($:= mN\Delta t$) is reached.

In simulations, we took $\Delta t = 1/[N(4J + h)]$ with $h = 0.025J$. For Figs. 2(b) and 2(c), we used $m = 2 \times 10^6$, ran 50 independent simulations, and took 51 samples from each simulation for averaging. For Figs. 3(a) and 3(c), we used $m = 10^6$ and ran 12000 independent simulations for averaging. For Figs. 4(b) and 4(c) as well as Fig. 12, we ran ten independent simulations for averaging. We explain the details of simulations for Fig. 5 in Appendix B 6. In all simulations, we set the disordered state with no spatial correlation as the initial state.

2. Langevin equation for spin-density field

Considering the ALG, we can obtain the probability density for a dynamical path of configurations $\{n_{j,s}(t)\}_{t \in [0, T]}$, where $n_{j,s}(t)$ is the occupancy of the site j and spin s at time t , as [60]

$$P[n_{j,s}] = \int D\tilde{n}_{j,s} \exp(-S[n_{j,s}, \tilde{n}_{j,s}]), \quad (\text{B1})$$

where $\int D\tilde{n}_{j,s}(\dots)$ is the functional integral over all the possible dynamical paths of the conjugate field $\{\tilde{n}_{j,s}(t)\}_{t \in [0, T]}$. Here, the action S is given as

$$\begin{aligned} S := & -i \int_0^T dt \sum_{j,s} \tilde{n}_{j,s} \partial_t n_{j,s} \\ & - \int_0^T dt \sum_{j,s} n_{j,s} \left\{ J \sum_k^{(j)} (1 - n_k) [e^{i(\tilde{n}_{j,s} - \tilde{n}_{k,s})} - 1] \right. \\ & \left. + h [e^{i(\tilde{n}_{j,s} - \tilde{n}_{j,-s})} - 1] \right\} \end{aligned}$$

$$\begin{aligned}
& - \int_0^T dt \sum_{j,s} n_{j,s} J \varepsilon_s \{ (1 - n_{j+\hat{x}}) [e^{i(\tilde{n}_{j,s} - \tilde{n}_{j+\hat{x},s})} - 1] \\
& - (1 - n_{j-\hat{x}}) [e^{i(\tilde{n}_{j,s} - \tilde{n}_{j-\hat{x},s})} - 1] \}, \quad (\text{B2})
\end{aligned}$$

where $\sum_k^{(j)}(\dots)$ is the summation over the sites adjacent to the site j . See Ref. [39] for the similar path-integral formulation [60] applied to the isotropic ALG.

Assuming that $\rho_s(\mathbf{r}, t) [:= n_{j,s}(t)]$ and $\tilde{\rho}_s(\mathbf{r}, t) [:= \tilde{n}_{j,s}(t)]$ are slowly varying on a scale of the lattice constant a , we approximate the action S up to $O(a^2)$. We also discard $O((\tilde{n}_{j,s} - \tilde{n}_{j,-s})^3)$ and higher-order terms to consider only the Gaussian noise in the resulting Langevin equation. Then, we can rewrite the action as $S \simeq S_{\text{cont}}^{(1)}[\rho_s, \tilde{\rho}_s] + S_{\text{cont}}^{(2)}[\rho_s, \tilde{\rho}_s]$, where

$$\begin{aligned}
S_{\text{cont}}^{(1)} & := -i \int_0^T dt \int \frac{d^2\mathbf{r}}{a^2} \sum_s \tilde{\rho}_s \{ \partial_t \rho_s - J a^2 (\nabla^2 \rho_s - \rho_{-s} \nabla^2 \rho_s \\
& + \rho_s \nabla^2 \rho_{-s}) + 2a\varepsilon J s \partial_x [(1 - \rho_+ - \rho_-) \rho_s] \\
& + h s (\rho_+ - \rho_-) \} \quad (\text{B3})
\end{aligned}$$

and

$$\begin{aligned}
S_{\text{cont}}^{(2)} & := \frac{1}{2} \int_0^T dt \int \frac{d^2\mathbf{r}}{a^2} \left[\sum_s 2J a^2 (1 - \rho_+ - \rho_-) \rho_s (\nabla \tilde{\rho}_s)^2 \right. \\
& \left. + h (\rho_+ + \rho_-) (\tilde{\rho}_+ - \tilde{\rho}_-)^2 \right]. \quad (\text{B4})
\end{aligned}$$

Introducing noise variables $\xi_s(\mathbf{r}, t)$, we transform the path probability $P[\rho_s]$, which is the continuum counterpart of $P[n_{i,s}]$, as [60]

$$P[\rho_s] = \int D\tilde{\rho}_s D\xi_s \exp(-S_{\text{cont}}^{(1)}[\rho_s, \tilde{\rho}_s] - S_{\text{cont}}^{(2')}[\rho_s, \tilde{\rho}_s, \xi_s]), \quad (\text{B5})$$

where

$$S_{\text{cont}}^{(2')} := \int_0^T dt \int \frac{d^2\mathbf{r}}{a^2} \left[\frac{1}{2} \sum_{s,s'} \xi_s (M^{-1})_{s,s'} \xi_{s'} + i \sum_s \tilde{\rho}_s \xi_s \right]. \quad (\text{B6})$$

Here, $M_{s,s'}$ is a differential operator given by $M_{s,s'} := \delta_{s,s'} [-2J \nabla \cdot (1 - \rho_+ - \rho_-) \rho_s \nabla] + (2\delta_{s,s'} - 1) h (\rho_+ + \rho_-)$. Following the approach developed by Martin, Siggia, Rose, Janssen, and de Dominicis (MSRJD) [61–63], we can obtain the Langevin equation that is equivalent to Eq. (B5) as

$$\begin{aligned}
\partial_t \rho_s & = J (\nabla^2 \rho_s - \rho_{-s} \nabla^2 \rho_s + \rho_s \nabla^2 \rho_{-s}) \\
& - 2\varepsilon J \partial_x [(1 - \rho_+ - \rho_-) \rho_s] - h (\rho_s - \rho_{-s}) + \xi_s, \quad (\text{B7})
\end{aligned}$$

where we set $a = 1$, $\xi_s(\mathbf{r}, t)$ is the Gaussian white noise with $\langle \xi_s(\mathbf{r}, t) \rangle = 0$, and $\langle \xi_s(\mathbf{r}, t) \xi_{s'}(\mathbf{r}', t') \rangle = a^2 \delta(t - t') M_{s,s'} \delta(\mathbf{r} - \mathbf{r}')$. This equation describes the stochastic dynamics of the coarse-grained variable, $\rho_s(\mathbf{r}, t)$.

3. Linearization of Langevin equation

Defining the total density $\rho_{\text{tot}}(\mathbf{r}, t) := \rho_+(\mathbf{r}, t) + \rho_-(\mathbf{r}, t)$ and the magnetization $m(\mathbf{r}, t) := \rho_+(\mathbf{r}, t) - \rho_-(\mathbf{r}, t)$, we can rewrite Eq. (2) [or (B7)] as

$$\partial_t \rho_{\text{tot}} = J \nabla^2 \rho_{\text{tot}} - 2\varepsilon J \partial_x [(1 - \rho_{\text{tot}}) m] + \xi_\rho \quad (\text{B8})$$

and

$$\begin{aligned}
\partial_t m & = J [(1 - \rho_{\text{tot}}) \nabla^2 m + m \nabla^2 \rho_{\text{tot}}] \\
& - 2\varepsilon J \partial_x [(1 - \rho_{\text{tot}}) \rho_{\text{tot}}] - 2hm + \xi_m. \quad (\text{B9})
\end{aligned}$$

Here, $\xi_\rho(\mathbf{r}, t) := \xi_+(\mathbf{r}, t) + \xi_-(\mathbf{r}, t)$ and $\xi_m(\mathbf{r}, t) := \xi_+(\mathbf{r}, t) - \xi_-(\mathbf{r}, t)$. Since m is a fast mode which decays exponentially according to the $-2hm$ term in Eq. (B9), we can set $\partial_t m = 0$ to examine long-time evolution of ρ_{tot} , which is a slow mode due to the particle number conservation.

Using the density fluctuation $\varphi(\mathbf{r}, t) := \rho_{\text{tot}}(\mathbf{r}, t) - \rho$, we can rewrite Eq. (B8) as

$$\partial_t \varphi = J \nabla^2 \varphi - 2\varepsilon J (1 - \rho) \partial_x m + 2\varepsilon J \partial_x (\varphi m) + \xi_\varphi. \quad (\text{B10})$$

Setting $\partial_t m = 0$ in Eq. (B9), we can linearize $m(\mathbf{r}, t)$ with respect to $\varphi(\mathbf{r}, t)$ as

$$m \simeq [2h - J(1 - \rho) \nabla^2]^{-1} [2\varepsilon J (2\rho - 1) \partial_x \varphi + \xi_m], \quad (\text{B11})$$

where we neglect the φ dependence of the noise [64–66]. Substituting Eq. (B11) into Eq. (B10), we can obtain the linearized equation of $\varphi(\mathbf{r}, t)$ as

$$\begin{aligned}
\partial_t \varphi & \simeq J \nabla^2 \varphi - 4\varepsilon^2 J^2 (1 - \rho) (2\rho - 1) \\
& \times [2h - J(1 - \rho) \nabla^2]^{-1} \partial_x^2 \varphi + \xi_\varphi, \quad (\text{B12})
\end{aligned}$$

where $\xi_\varphi := \xi_\rho - 2\varepsilon J (1 - \rho) [2h - J(1 - \rho) \nabla^2]^{-1} \partial_x \xi_m$, $\langle \xi_\varphi(\mathbf{r}, t) \rangle = 0$, and

$$\begin{aligned}
\langle \xi_\varphi(\mathbf{r}, t) \xi_\varphi(\mathbf{r}', t') \rangle & = -2J(1 - \rho) \rho \nabla^2 \delta(\mathbf{r} - \mathbf{r}') \delta(t - t') \\
& - 8\varepsilon^2 J^2 (1 - \rho)^2 \rho [2h - J(1 - \rho) \nabla^2]^{-1} \partial_x^2 \delta(\mathbf{r} - \mathbf{r}') \delta(t - t'). \quad (\text{B13})
\end{aligned}$$

Applying Fourier transformation, $\varphi(\mathbf{k}, t) := \int d^2\mathbf{r} \exp(-i\mathbf{k} \cdot \mathbf{r}) \varphi(\mathbf{r}, t)$, we can solve Eq. (B12) and finally obtain the structure factor, $S_{\text{lin}}(\mathbf{k}) := (L_x L_y)^{-1} \lim_{t \rightarrow \infty} \langle |\varphi(\mathbf{k}, t)|^2 \rangle$,

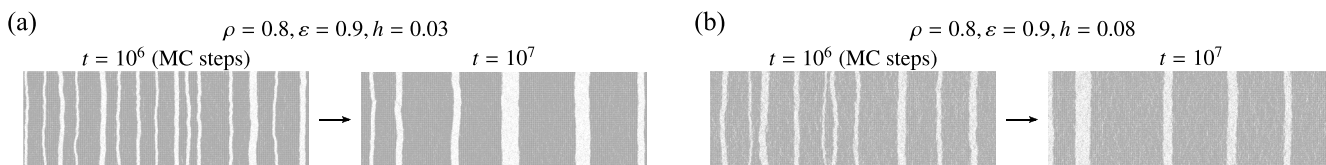


FIG. 13. Typical time evolution of the ALG with $(L_x, L_y) = (1200, 400)$ for (a) $\rho = 0.8$, $\varepsilon = 0.9$, and $h = 0.03$; (b) $\rho = 0.8$, $\varepsilon = 0.9$, and $h = 0.08$.

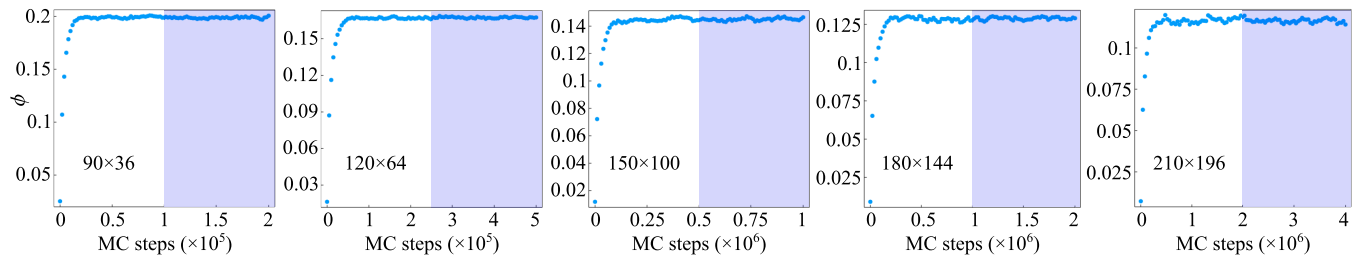


FIG. 14. Time dependence of the order parameter ϕ averaged over independent simulations for $\rho = 0.6$ and $\varepsilon = 0.362 (\simeq \varepsilon_c)$. The number of performed independent simulations is 10000 for $(L_x, L_y) = (90, 36)$ and $(120, 64)$; 4000 for $(L_x, L_y) = (150, 100)$; 2000 for $(L_x, L_y) = (180, 144)$; 1000 for $(L_x, L_y) = (210, 196)$. For further averaging, we took 51 samples from the time region with purple color at equal intervals.

as

$$S_{\text{lin}}(\mathbf{k}) = (1 - \rho)\rho \times \frac{[2h + J(1 - \rho)\mathbf{k}^2]\mathbf{k}^2 + 4\varepsilon^2 J(1 - \rho)\mathbf{k}_x^2}{[2h + J(1 - \rho)\mathbf{k}^2]\mathbf{k}^2 - 4\varepsilon^2 J(1 - \rho)(2\rho - 1)\mathbf{k}_x^2}. \quad (\text{B14})$$

4. Anisotropic growth in PS state

In Fig. 12, We show the space and time dependence of the density correlation function for $(\rho, \varepsilon) = (0.4, 0.9)$ and $(0.6, 0.6)$, which are different from the parameters used for Fig. 4. We can see that the anisotropic power law of the typical domain size, $R_x(t) \sim t^{\alpha_x}$ and $R_y(t) \sim t^{\alpha_y}$ with $\alpha_x < \alpha_y$, holds both for $(\rho, \varepsilon) = (0.4, 0.9)$ and $(0.6, 0.6)$ as observed for $(\rho, \varepsilon) = (0.6, 0.9)$ (Fig. 4), though the exponent seems nonuniversal.

To examine whether the counterpart of the bubbly phase separation, which has been observed in the isotropic ALG [44], can appear in the anisotropic ALG, we performed simulations using systems with $(L_x, L_y) = (1200, 400)$. We did not find evidence of an analog of the bubbly phase separation, where the bubbles of the low-density phase should be nucleated inside the bulk high-density phase, though the steady state has not been reached by the end of the simulation (10^7 MC steps) [see Figs. 13(a) and 13(b) for typical snapshots for $(\rho, \varepsilon, h) = (0.8, 0.9, 0.03)$ and $(0.8, 0.9, 0.08)$, respectively].

5. Effective model for critical dynamics

Setting $\partial_t m = 0$ by focusing on long-time evolution and using $\varphi(\mathbf{r}, t) = \rho_{\text{tot}}(\mathbf{r}, t) - \rho$ as in Appendix B 3, we can iteratively solve Eq. (B9) as

$$\begin{aligned} m &= \frac{1}{2h} [2\varepsilon J(2\rho - 1)\partial_x \varphi + 2\varepsilon J\partial_x \varphi^2 + \xi_m] \\ &+ \frac{J}{2h} [(1 - \rho)\nabla^2 m + \nabla \cdot (-\varphi \nabla m + m \nabla \varphi)] \\ &= \frac{1}{2h} [2\varepsilon J(2\rho - 1)\partial_x \varphi + 2\varepsilon J\partial_x \varphi^2 + \xi_m] \\ &+ \frac{J}{4h^2} (1 - \rho) [2\varepsilon J(2\rho - 1)\nabla^2 \partial_x \varphi] \\ &+ O(\nabla^4 \partial_x \varphi, \nabla^2 \partial_x \varphi^2, \nabla^2 \xi_m). \end{aligned} \quad (\text{B15})$$

Substituting Eq. (B15) into Eq. (B10), we can obtain

$$\begin{aligned} \partial_t \varphi &= J \left[1 - \frac{2\varepsilon^2 J}{h} (1 - \rho)(2\rho - 1) \right] \partial_x^2 \varphi + J \partial_y^2 \varphi \\ &- \frac{\varepsilon^2 J^3}{h^2} (1 - \rho)^2 (2\rho - 1) \partial_x^4 \varphi \\ &+ \frac{\varepsilon^2 J^2}{h} (4\rho - 3) \partial_x^2 \varphi^2 + \frac{4\varepsilon^2 J^2}{3h} \partial_x^2 \varphi^3 \\ &+ \sqrt{2J(1 - \rho)\rho} \left[1 + \frac{2\varepsilon^2 J}{h} (1 - \rho) \right] \partial_x \eta \\ &+ O(\partial_x^2 \partial_y^2 \varphi, \partial_x^6 \varphi, \partial_x^4 \varphi^2, \partial_y \eta, \partial_x^2 \eta, \sqrt{\varphi} \partial_x \eta), \end{aligned} \quad (\text{B16})$$

where $\eta(\mathbf{r}, t)$ satisfies $\langle \eta(\mathbf{r}, t) \rangle = 0$ and $\langle \eta(\mathbf{r}, t) \eta(\mathbf{r}', t') \rangle = \delta(\mathbf{r} - \mathbf{r}') \delta(t - t')$. Note that, neglecting the noise η , we can obtain the spinodal line $\varepsilon_{\text{sp}}(\rho)$ from $1 = 2\varepsilon_{\text{sp}}(\rho)^2 J(1 - \rho)(2\rho - 1)/h$ and the mean-field critical point as $\rho_c^{\text{MF}} = 3/4$ and $\varepsilon_c^{\text{MF}} = \pm 2\sqrt{h/J}$.

Applying the MSRJD approach to Eq. (B16), we can show that the probability density for a dynamical path of configurations $\{\varphi(t)\}_{t \in [0, T]}$ is given by

$$P[\varphi] = \int D(i\tilde{\varphi}) \exp(-S_\varphi[\varphi, \tilde{\varphi}]). \quad (\text{B17})$$

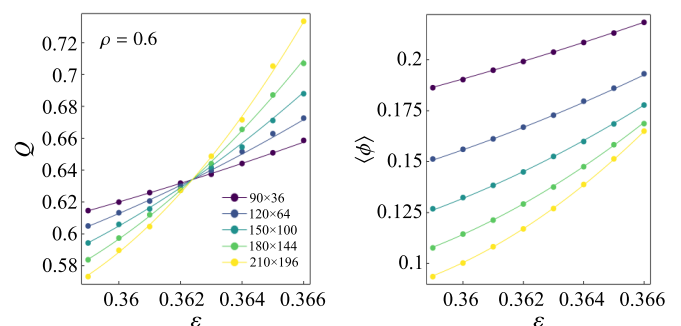


FIG. 15. The Binder cumulant Q and the order parameter $\langle \phi \rangle$ obtained from simulations (colored dots), which correspond to Figs. 5(a) and 5(b), and the best-fitted curves (colored lines).

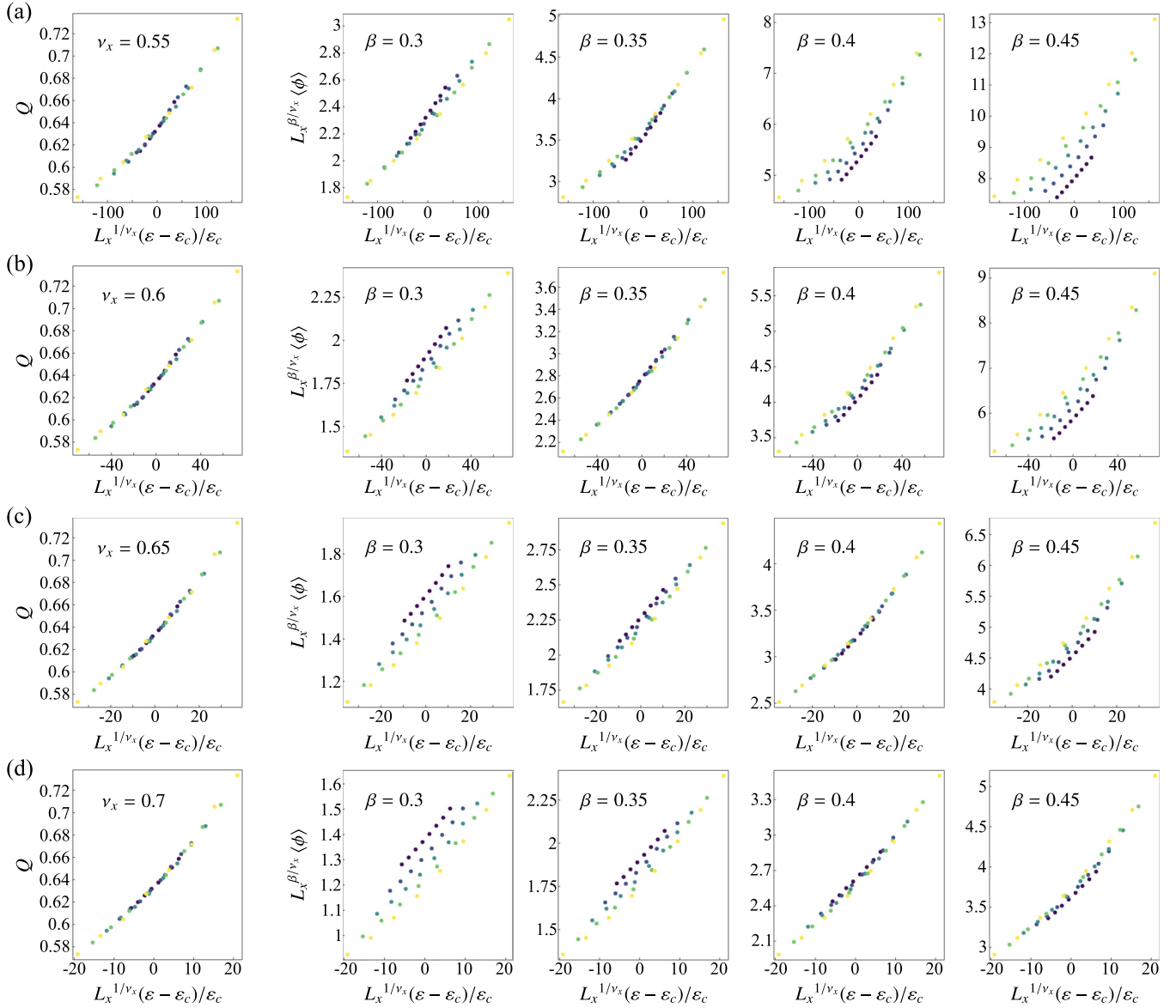


FIG. 16. Rescaled Q and $\langle \phi \rangle$ for the best-fitted parameters with ν_x and β fixed: (a) $\nu_x = 0.55$ and $\beta = 0.3$ – 0.45 , (b) $\nu_x = 0.6$ and $\beta = 0.3$ – 0.45 , (c) $\nu_x = 0.65$ and $\beta = 0.3$ – 0.45 , and (d) $\nu_x = 0.7$ and $\beta = 0.3$ – 0.45 . We used the same simulation data as in Fig. 5, and the best-fitted critical point is $\varepsilon_c \simeq 0.362$ for (a) through (d).

Here, the action is given by

$$S_\varphi := \int_0^T dt \int d^2r [\tilde{\varphi}(\partial_t \varphi - \tau_x \partial_x^2 \varphi - \tau_y \partial_y^2 \varphi + a \partial_x^4 \varphi - v \partial_x^2 \varphi^2 - u \partial_x^2 \varphi^3) + c \tilde{\varphi} \partial_x^2 \tilde{\varphi} + (\text{h.o.t.})], \quad (\text{B18})$$

where we generalize the coupling constants for each term in Eq. (B16) as $J[1 - 2\varepsilon^2 J(1 - \rho)(2\rho - 1)/h] \rightarrow \tau_x$, $J \rightarrow \tau_y$, $\varepsilon^2 J^3(1 - \rho)^2(2\rho - 1)/h^2 \rightarrow a$, $\varepsilon^2 J^2(4\rho - 3)/h \rightarrow v$, $4\varepsilon^2 J^2/(3h) \rightarrow u$, and $J(1 - \rho)\rho[1 + 2\varepsilon^2 J(1 - \rho)/h] \rightarrow c$. In Eq. (B18), (h.o.t.) corresponds to the higher-order terms in Eq. (B16), which are irrelevant in the renormalization group (RG) sense, as shown below.

We consider the tree-level RG analysis for Eq. (B18). Considering the scale transformation $x \rightarrow b^{-1}x$ ($b > 1$) and requiring the invariance of τ_y , a , and c under the

transformation, we can obtain the scaling of other quantities as

$$\begin{aligned} y &\rightarrow b^{-2}y \\ t &\rightarrow b^{-4}t \\ \varphi &\rightarrow b^{1/2}\varphi \\ \tilde{\varphi} &\rightarrow b^{5/2}\tilde{\varphi}, \\ \tau_x &\rightarrow b^2\tau_x \\ v &\rightarrow b^{5/2}v \\ u &\rightarrow bu \end{aligned} \quad (\text{B19})$$

suggesting that τ_x , v , and u are relevant variables. In particular, $\tau_x \propto (\varepsilon - \varepsilon_c)$ around the critical point. Further, we can write each term of (h.o.t.) in Eq. (B18) as $d_{\gamma_x \gamma_y \gamma_\varphi} \tilde{\varphi} \partial_x^{\gamma_x} \partial_y^{\gamma_y} \varphi^{\gamma_\varphi}$ or $e_{\delta_x \delta_y \delta_\varphi} \tilde{\varphi} \partial_x^{\delta_x} \partial_y^{\delta_y} \varphi^{\delta_\varphi} \tilde{\varphi}$, and the scaling of the coupling constants is

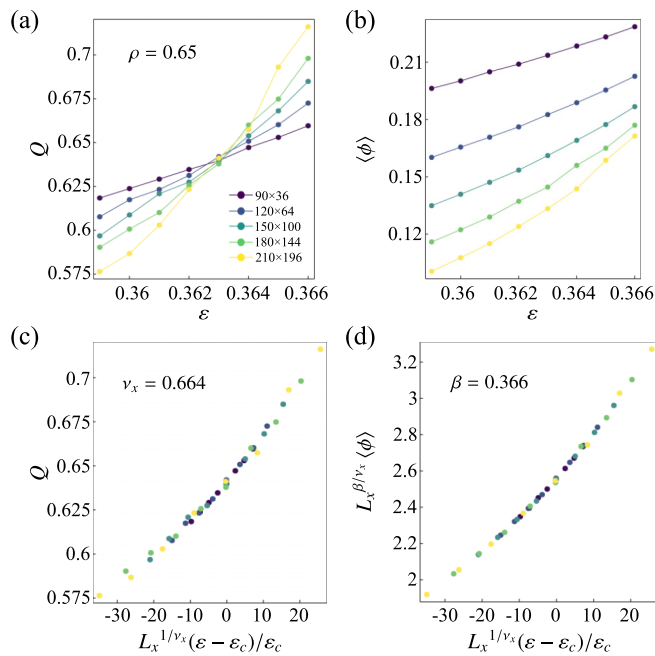


FIG. 17. Counterparts of Fig. 5 for $\rho = 0.65$ with $L_y/L_x^2 = 1/15^2$. (a) ε and system size dependence of the Binder ratio Q . The solid lines are guides for the eyes. (b) ε and system size dependence of $\langle \phi \rangle$. (c) Q as a function of the rescaled ε with the best-fitted ε_c ($\simeq 0.363$) and ν_x ($\simeq 0.664$). (d) Rescaled $\langle \phi \rangle$ as a function of the rescaled ε with the best-fitted β ($\simeq 0.366$) and the same values of ε_c and ν_x as (c).

obtained as

$$\begin{aligned} d_{\gamma_x \gamma_y \gamma_\varphi} &\rightarrow b^{9/2 - \gamma_x - 2\gamma_y - \gamma_\varphi/2} d_{\gamma_x \gamma_y \gamma_\varphi} \\ e_{\delta_x \delta_y \delta_\varphi} &\rightarrow b^{2 - \delta_x - 2\delta_y - \delta_\varphi/2} e_{\delta_x \delta_y \delta_\varphi}. \end{aligned} \quad (\text{B20})$$

Since $\gamma_x + 2\gamma_y + \gamma_\varphi/2 \geq 5$ and $\delta_x + 2\delta_y + \delta_\varphi/2 \geq 5/2$, $d_{\gamma_x \gamma_y \gamma_\varphi}$ and $e_{\delta_x \delta_y \delta_\varphi}$ are irrelevant variables.

Omitting the irrelevant variables and adjusting the density ρ so that $v = 0$ in Eq. (B18), we obtain the effective action for the critical dynamics of the ALG,

$$\begin{aligned} S'_\varphi := \int_0^T dt \int d^2r [\tilde{\varphi}(\partial_t \varphi - \tau_x \partial_x^2 \varphi - \tau_y \partial_y^2 \varphi + a \partial_x^4 \varphi \\ - u \partial_x^2 \varphi^3) + c \tilde{\varphi} \partial_x^2 \tilde{\varphi}], \end{aligned} \quad (\text{B21})$$

which coincides with that of the two-temperature lattice gas model [68–71].

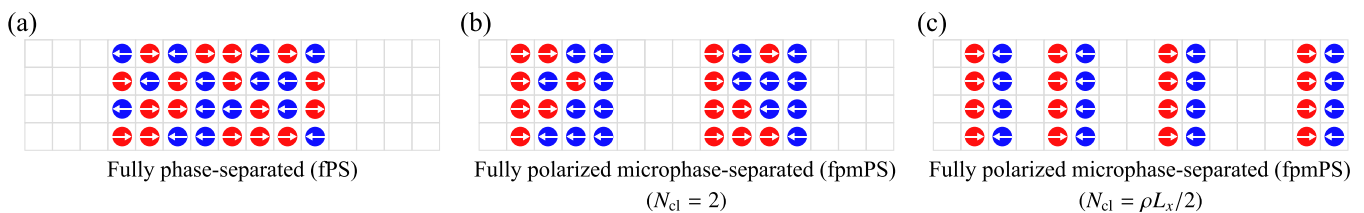


FIG. 18. Schematic figures of representative states. (a) In the FPS state, a single cluster with random spins is formed and its circumference is minimized. (b) In the fpmPS state, there are N_{cl} clusters with oppositely polarized edges. (c) For large enough U_2 ($\gg J, h, U_1$), the fpmPS state is stable with the maximal number of clusters, $N_{\text{cl}} = \rho L_x/2$.

6. Finite-size scaling analysis

For Fig. 5, we performed 1000–10000 independent simulations and took 51 samples from each simulation for averaging. In Fig. 14, we show the time dependence of the order parameter ϕ averaged over independent simulations for $\varepsilon = 0.362$ ($\simeq \varepsilon_c$) and the time region used for further averaging. Similar time dependence was obtained also for other values of ε .

To find the critical point ε_c and the critical exponents ν_x and β from the obtained data [Figs. 5(a) and 5(b)], we performed curve fitting with a Julia package LsqFit.jl. We first fitted the data of the Binder ratio $Q(\varepsilon, L_x)$ with the formula, $Q^{(0)} + Q^{(1)}L_x^{1/\nu_x}(\varepsilon - \varepsilon_c) + Q^{(2)}L_x^{2/\nu_x}(\varepsilon - \varepsilon_c)^2$, based on the second-order expansion of the scaling form $Q(\varepsilon, L_x) = F_Q(L_x^{1/\nu_x}(\varepsilon - \varepsilon_c))$. Here, the fitting parameters are $Q^{(0)}$, $Q^{(1)}$, $Q^{(2)}$, ε_c , and ν_x . Then, using the obtained ε_c and ν_x , we fitted the data of $\langle \phi \rangle(\varepsilon, L_x)$ with the formula, $\phi^{(0)}L_x^{-\beta/\nu_x} + \phi^{(1)}L_x^{-\beta/\nu_x + 1/\nu_x}(\varepsilon - \varepsilon_c) + \phi^{(2)}L_x^{-\beta/\nu_x + 2/\nu_x}(\varepsilon - \varepsilon_c)^2$, based on the second-order expansion of the scaling form $\langle \phi \rangle(\varepsilon, L_x) = L_x^{-\beta/\nu_x} F_1(L_x^{1/\nu_x}(\varepsilon - \varepsilon_c))$. Here, the fitting parameters are $\phi^{(0)}$, $\phi^{(1)}$, $\phi^{(2)}$, and β . We show the best-fitted curves for $Q(\varepsilon, L_x)$ and $\langle \phi \rangle(\varepsilon, L_x)$ in Fig. 15, and the best-fitted parameters are $\varepsilon_c \simeq 0.36238(4)$, $\nu_x \simeq 0.65(1)$, and $\beta \simeq 0.3928(8)$ as mentioned in Sec. III C, where the value in the bracket is the fitting error on the last significant figure.

To check the deviation of the scaling behavior against slight changes in the estimated critical exponents, we also tried another curve fitting with ν_x and β fixed. Here, the fitting formulas are the same as before, but the fitting parameters are $(Q^{(0)}, Q^{(1)}, Q^{(2)}, \varepsilon_c)$ in fitting $Q(\varepsilon, L_x)$ and $(\phi^{(0)}, \phi^{(1)}, \phi^{(2)})$ in fitting $\langle \phi \rangle(\varepsilon, L_x)$. Plotting the rescaled curves similarly to Figs. 5(c) and 5(d) for several values of ν_x and β (Fig. 16), we find that the curves seem well-scaled for a certain range of exponents, including $(\nu_x, \beta) = (0.6, 0.35)$, which, within uncertainty, coincide with those observed for the two-temperature lattice gas model [71].

We further performed MC simulations and the finite-size scaling analysis for $\rho = 0.65$ with $S = L_y/L_x^2 = 1/15^2$ in the same way as for $\rho = 0.6$. The counterparts of Fig. 5 for $\rho = 0.65$ are shown in Fig. 17. The best-fitted parameters are $\varepsilon_c = 0.36304(7)$, $\nu_x = 0.66(2)$, and $\beta = 0.366(1)$, which are qualitatively similar to the case of $\rho = 0.6$, given the well-scaled range of exponents for $\rho = 0.6$ (Fig. 16).

APPENDIX C: DIFFUSION MONTE CARLO SIMULATION

For the quantum model [Eq. (1)], we first divide the Hamiltonian into two parts $H = -W - D$, where W is given by (A1)

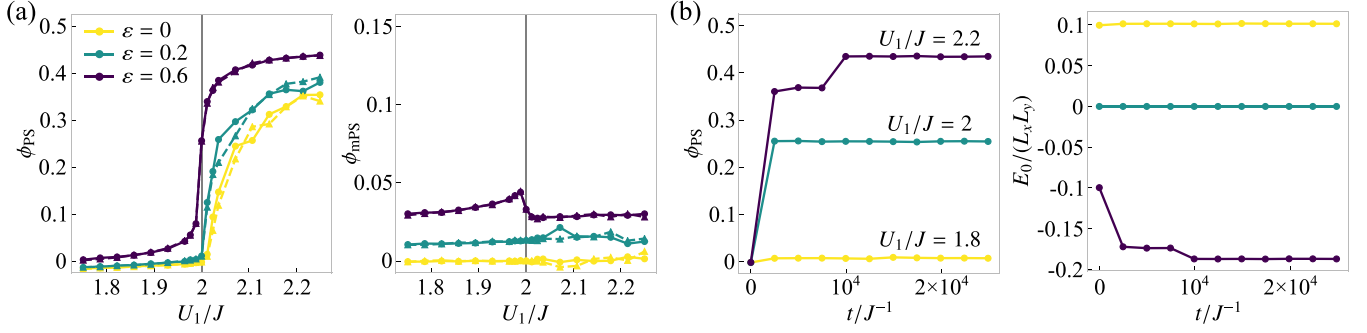


FIG. 19. (a) U_1 dependence of the order parameters, ϕ_{PS} and ϕ_{mPS} , obtained with the disordered (solid line with circles) or the PS (dashed line with triangles) initial state for $\epsilon = 0, 0.2, 0.6$. (b) Time evolution of ϕ_{PS} and E_0 in simulations, obtained with the disordered initial state for $\epsilon = 0.6$ and $U_1/J = 1.8, 2$, and 2.2 . In both (a) and (b), we considered 50×5 systems and used $\rho = 0.5$, $h = 0.025J$, and $U_2 = \epsilon J$. Simulation parameters are $\Delta t = 1/[N(4J + h)]$, $N_c = 5 \times 10^3$, and $M = 10^5 N$ as used in Fig. 6(a) of the main text (see Appendix C). Note that, since we set $\hbar = 1$, time and inverse of energy have the same dimension.

and D is diagonal in the Fock space. To numerically calculate the quantity $\langle A \rangle_C = \langle P|A(\{\hat{n}_{i,s}\})|\psi_0\rangle / \langle P|\psi_0\rangle$ for the ground state $|\psi_0\rangle$, we transform $\langle A \rangle_C$ as

$$\begin{aligned} \langle A \rangle_C &= \lim_{T \rightarrow \infty} \frac{\langle P|A(\{\hat{n}_{i,s}\})e^{(W+D)T}|\psi_{\text{ini}}\rangle}{\langle P|e^{(W+D)T}|\psi_{\text{ini}}\rangle} \\ &= \lim_{T \rightarrow \infty} \frac{\sum_{C,C_0} A(C) \langle C|e^{(W+D)T}|C_0\rangle P_{\text{ini}}(C_0)}{\sum_{C,C_0} \langle C|e^{(W+D)T}|C_0\rangle P_{\text{ini}}(C_0)}, \quad (\text{C1}) \end{aligned}$$

where $|\psi_{\text{ini}}\rangle := \sum_C P_{\text{ini}}(C)|C\rangle$ with $P_{\text{ini}}(C) \geq 0$ is an arbitrary initial state. Instead of taking $T \rightarrow \infty$, we consider a finite but large enough T for the initial state to relax to the ground state.

Splitting the total time T as $T = M\Delta t$ with a time step $\Delta t [= O(N^{-1})]$ and writing $C = C_M$ for convenience, we can divide the time evolution into small steps:

$$\begin{aligned} \langle C|e^{(W+D)T}|C_0\rangle &= \sum_{C_1, \dots, C_{M-1}} \prod_{m=1}^M \langle C_m|e^{(W+D)\Delta t}|C_{m-1}\rangle \\ &\approx \sum_{C_1, \dots, C_{M-1}} \prod_{m=1}^M (\delta_{C_m, C_{m-1}} + W_{C_m, C_{m-1}} \Delta t)(1 + D_{C_{m-1}} \Delta t), \quad (\text{C2}) \end{aligned}$$

where $D_C := \langle C|D|C\rangle$ and the approximation in the third line is correct up to $O(\Delta t)$. Since $\delta_{C_m, C_{m-1}} + W_{C_m, C_{m-1}} \Delta t$ is a stochastic matrix for the ALG, we can approximately calculate (C2) by assigning the weight $\prod_{m=1}^M (1 + D_{C_{m-1}} \Delta t)$ to the sampled path $C_0 \rightarrow C_1 \rightarrow \dots \rightarrow C_M$ in the Monte Carlo (MC) simulations of the ALG.

To efficiently sample the configurations that have high probability weights but rarely appear in the MC simulation, we use the resampling technique [74]. We consider a set of configurations, $\{C_m^{(i)}\}_{i=1}^{N_c}$, which evolve independently through the MC dynamics, where N_c is the total number of clones. Correspondingly, we introduce a set of cumulative weights, $\{w_m^{(i)}\}_{i=1}^{N_c}$, according to the paths $\{C_0^{(i)} \rightarrow \dots \rightarrow C_m^{(i)}\}_{i=1}^{N_c}$. Whenever the effective sample size [94], $(\sum_{i=1}^{N_c} w_m^{(i)})^2 / \sum_{i=1}^{N_c} (w_m^{(i)})^2$, becomes smaller than $0.5N_c$

during the MC dynamics, we perform resampling of configurations from the distribution of $\{C_m^{(i)}\}_{i=1}^{N_c}$ weighted by $\{w_m^{(i)}\}_{i=1}^{N_c}$ and then reset the weights as $w_m^{(i)} = 1$ for all i . Using the final-time configurations and weights, $\{C_M^{(i)}\}_{i=1}^{N_c}$ and $\{w_M^{(i)}\}_{i=1}^{N_c}$, we estimate $\langle A \rangle_C$ as

$$\langle A \rangle_C \approx \frac{\sum_{i=1}^{N_c} w_M^{(i)} A(C_M^{(i)})}{\sum_{i=1}^{N_c} w_M^{(i)}}. \quad (\text{C3})$$

In 2D simulations, we typically took $\Delta t = 1/[N(4J + h)]$ and used $(N_c, M) = (5 \times 10^3, 10^5 N)$ for Fig. 6(a); $(N_c, M) = (10^5, 10^4 N)$ for Figs. 6(b) and 7(a); and $(N_c, M) = (2 \times 10^4, 2 \times 10^4 N)$ for Fig. 8. Here, we took large clone numbers to reduce possible systematic errors (see [95,96] for systematic errors in the DMC and comparisons with exact results). In 1D simulations for Fig. 7(b), we took $\Delta t = 1/[N(2J + h)]$ and $(N_c, M) = (10^5, 10^4 N)$ (see Fig. 20 for the N_c dependence in small 1D systems). In all simulations, we set the disordered state with no spatial correlation as the initial state, while we confirmed that there is no qualitative dependence on the initial state (see Appendix D 5).

APPENDIX D: PROPERTIES OF THE MODEL AND DETAILS OF THE ANALYSIS

1. Generalized quantum model and classical condition

We consider a generalized version of the two-component hard-core boson model (1) in the main text:

$$\begin{aligned} H_{\text{gen}} &= \hat{P} \left(- \sum_i \sum_{l=x,y} \sum_{s,r=\pm} J_{s,r}^{(l)} a_{i+r\hat{l},s}^\dagger a_{i,s} - \sum_i \sum_{a=0,1,2,3} \sum_{s,s'=\pm} \right. \\ &\quad \left. \times h_a \sigma_{s,s'}^a a_{i,s}^\dagger a_{i,s'} - \sum_i \sum_{l=x,y} \sum_{s,r=\pm} U_{s,r}^{(l)} \hat{n}_{i,s} \hat{n}_{i+r\hat{l}} \right) \hat{P}, \quad (\text{D1}) \end{aligned}$$

where σ^0 is the 2×2 identity matrix, σ^a ($a = 1, 2, 3$) are the Pauli matrices, and \hat{P} is the projection to a partial Fock space where the total particle number is N with no multiple occupancy. We assume $[a_{i,s}, a_{j,s'}^\dagger] = [a_{i,s}, a_{j,s'}] = [a_{i,s}^\dagger, a_{j,s'}^\dagger] = 0$

for $(i, s) \neq (j, s')$; $\{a_{i,s}, a_{i,s}^\dagger\} = 1$ and $a_{i,s}^2 = (a_{i,s}^\dagger)^2 = 0$. The first term of Eq. (D1) represents hopping, which is, in general, non-Hermitian and dependent on the spin and/or the hopping direction. The second and third terms represent the effect of external fields and the generalized nearest-neighbor interactions, respectively. For $J_{s,r}^{(l)} = (1 + sr\varepsilon\delta_{l,x})J$, $h_a = -(4J + h)\delta_{a,0} + h\delta_{a,1}$, and $U_{s,r}^{(l)} = U_1/2 + srU_2\delta_{l,x}$, we can reproduce the model (1) in the main text.

Here, we take $U_{s,r}^{(l)} = J_{s,r}^{(l)}$, $h_0 = -\sum_{l,s,r} J_{s,r}^{(l)}/2 - h_1$, $h_2 = 0$, and $h_3 = -\sum_{l,s,r} sJ_{s,r}^{(l)}/2$ with arbitrary $J_{s,r}^{(l)} > 0$ and $h_1 > 0$, which is the generalized classical condition (see the main text and Appendix A). Defining $W := -H_{\text{gen}}$ under this clas-

sical condition, we can obtain

$$W = \hat{P} \left\{ \sum_i \sum_{l=x,y} \sum_{s,r=\pm} J_{s,r}^{(l)} [a_{i+r\hat{l},s}^\dagger a_{i,s} - \hat{n}_{i,s}(1 - \hat{n}_{i+r\hat{l}})] + \sum_{i,s=\pm} h_1 (a_{i,s}^\dagger a_{i,-s} - \hat{n}_{i,s}) \right\} \hat{P}. \quad (\text{D2})$$

Defining $W_{C,C'} := \langle C|W|C' \rangle$, where $|C\rangle$ is the Fock basis, we can show that (i) $\sum_C W_{C,C'} = 0$ and (ii) $W_{C,C'} \geq 0$ for $C \neq C'$, and thus we can interpret $W_{C,C'}$ as a transition rate matrix of a classical Markov process. Under this interpretation, $J_{s,r}^{(l)}$ is

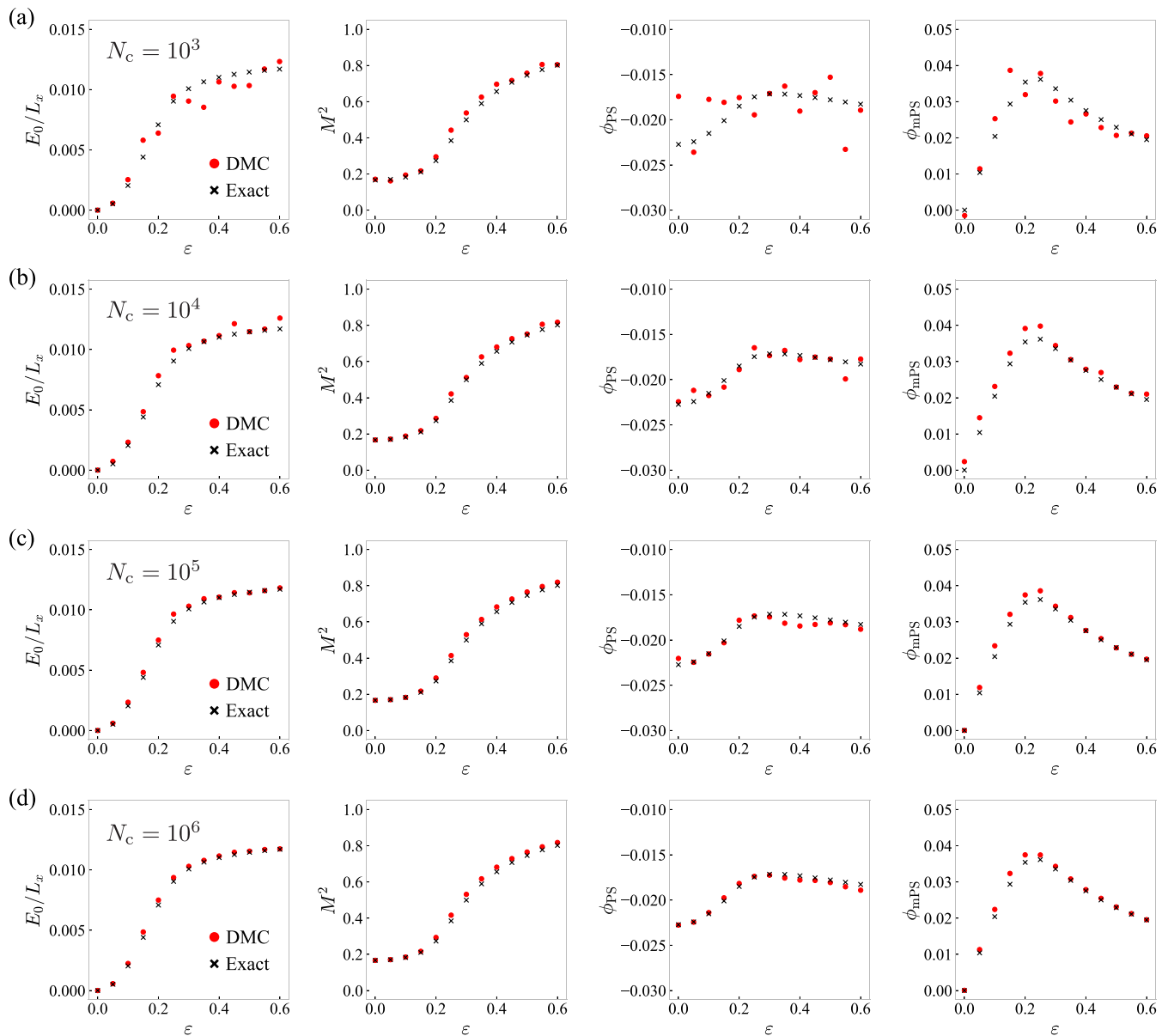


FIG. 20. Comparison of the results obtained by DMC simulations (red dots) and exact diagonalization (black crosses) for small 1D systems with $L_x = 12$, $\rho = 0.5$, $h = 0.025J$, $U_1 = 2J$, and $U_2 = 0$. From left to right, we plot the ground-state energy, squared magnetization, and order parameters for phase separation and microphase separation. Each row corresponds to the different number of clones used in DMC simulations: (a) $N_c = 10^3$, (b) 10^4 , (c) 10^5 , and (d) 10^6 . The simulation parameters are $\Delta t = 1/[N(2J + h)]$ and $M = 10^4N$. Note that the parameters used in (c) are the same as those for Fig. 7(b), except for the system size.

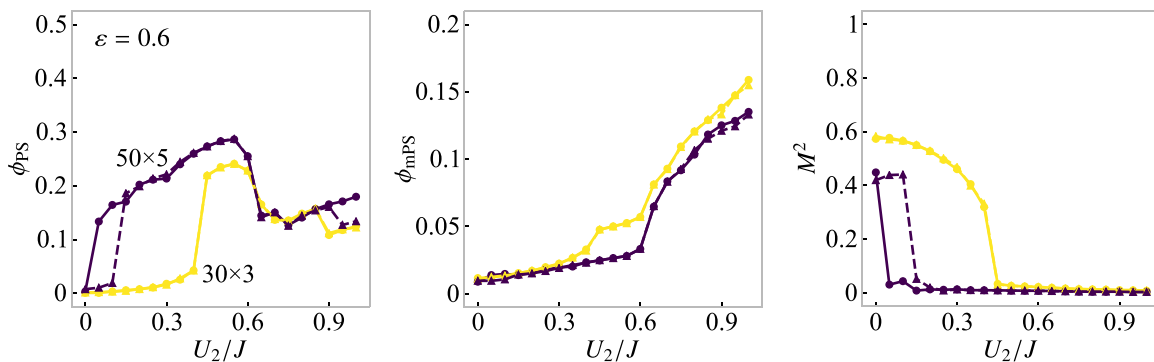


FIG. 21. U_2 dependence of ϕ_{PS} , ϕ_{mPS} , and M^2 . We used $\rho = 0.5$, $\varepsilon = 0.6$, $h = 0.025J$, and $U_1 = 2J$ in 30×3 and 50×5 systems, with the PS (solid line with circles) or the polar (dashed line with triangles) initial state. Simulation parameters are $\Delta t = 1/[N(4J + h)]$, $N_c = 10^5$, and $M = 10^4 N$.

the hopping rate of a particle with spin s from a site i to the adjacent site $i + r\hat{l}$, and h_1 is the spin flipping rate.

Lastly, we briefly discuss the quantum model (1) in the main text for the open boundary condition (OBC). OBC in a quantum system is when the hopping to the outside of the $L_x \times L_y$ region (Ω) is prohibited and there are no interactions between the particles inside and the outside of Ω . This is different to the OBC in the classical system such as in ALG, meaning that there is no classical line in the case of OBC. We conducted exact diagonalization calculations for a small 1D quantum system to check the effect of this open boundary condition on the phase diagram (see Appendix E and Fig. 25 for more details). On the other hand, we can think of a quantum system that corresponds to the ALG with OBC by setting $U_1 = 2J$ and $U_2 = \varepsilon J$ and adding a boundary term: $W_{C,C'} = -\langle C|H + H_{\text{bd}}|C'\rangle$ with $H_{\text{bd}} := -J\hat{P}[\sum_{i \in \partial\Omega \setminus \partial\partial\Omega} \hat{n}_i + 2\sum_{i \in \partial\partial\Omega} \hat{n}_i + \varepsilon \sum_{j=1}^{L_y} (\hat{m}_{L_x, \hat{x}+j\hat{y}} - \hat{m}_{1, \hat{x}+j\hat{y}})]\hat{P}$. Here we denoted the boundary points of Ω as $\partial\Omega$ and the four corner points as $\partial\partial\Omega$.

2. Correspondence to the ferromagnetic XXZ model

We consider the case where $\varepsilon = 0$ and $U_2 = 0$. Since there is no spin dependence in this model, it is equivalent to the

single-component hard-core boson model ($J > 0$ and $U_1 > 0$):

$$H_{\text{HCB}} = -J \sum_{(i,j)} (a_i^\dagger a_j + a_j^\dagger a_i) - U_1 \sum_{(i,j)} \hat{n}_i \hat{n}_j + \text{const.} \quad (\text{D3})$$

Mapping the Fock bases to spin-1/2 bases as $|n_j = 0\rangle \rightarrow |s_j^z = -1/2\rangle$ and $|n_j = 1\rangle \rightarrow |s_j^z = +1/2\rangle$, or equivalently, $a_j \rightarrow \hat{S}_j^-$ and $a_j^\dagger \rightarrow \hat{S}_j^+$ with $\hat{S}_j^\pm := \hat{S}_j^x \pm i\hat{S}_j^y$, we obtain

$$H_{\text{HCB}} \rightarrow H_{\text{XXZ}} = - \sum_{(i,j)} [2J(\hat{S}_i^x \hat{S}_j^x + \hat{S}_i^y \hat{S}_j^y) + U_1 \hat{S}_i^z \hat{S}_j^z] + \text{const.} \quad (\text{D4})$$

For $U_1 > 0$, H_{XXZ} represents the ferromagnetic XXZ model. Here, the total particle number N and the system size $L_x L_y$ in the hard-core boson model are related to the total magnetization M_{tot}^z in the XXZ model as $M_{\text{tot}}^z = N - L_x L_y / 2$. In particular, when $U_1 = 2J$, H_{XXZ} is nothing but the ferromagnetic Heisenberg Hamiltonian [72].

3. Lower bound of the ground state energy

As in Sec. IV and Appendix C, we divide the Hamiltonian into two parts as $H = -W - D$, where W is the classical

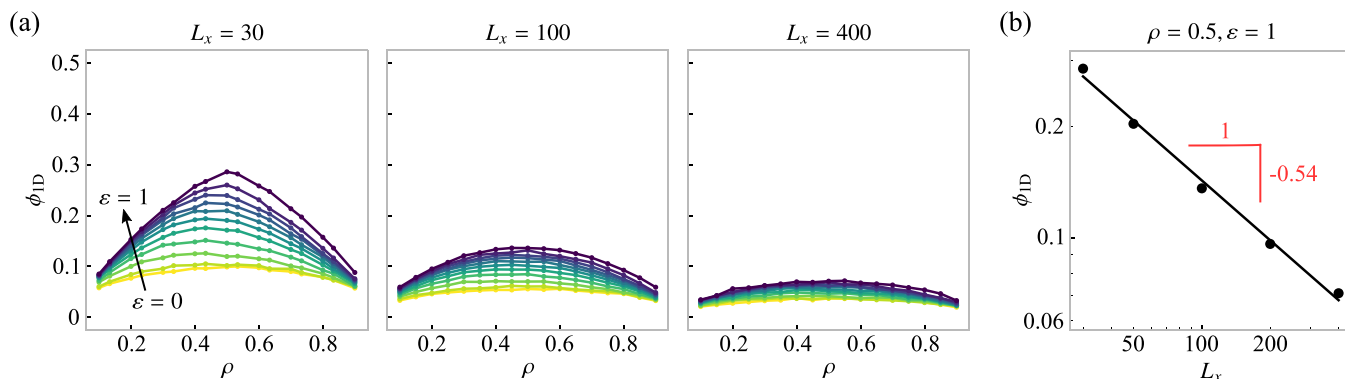


FIG. 22. (a) ρ dependence of $\phi_{1\text{D}}$ for different values of ε (in increments of 0.1) in the 1D ALG with $L_x = 30$, 100, and 400. (b) L_x dependence of $\phi_{1\text{D}}$ for $\rho = 0.5$ and $\varepsilon = 1$, which indicates $\phi_{1\text{D}} \sim L_x^{-0.54}$ for large L_x . In both (a) and (b), we used $h = 0.05J$. Also, we used $\Delta t = 1/[N(2J + h)]$ and took 10^4 samples with $M = 10^4 N$ for $L_x = 30, 50, 100$; 5×10^3 samples with $M = 2 \times 10^4 N$ for $L_x = 200$; and 3×10^3 samples with $M = 5 \times 10^4 N$ for $L_x = 400$.

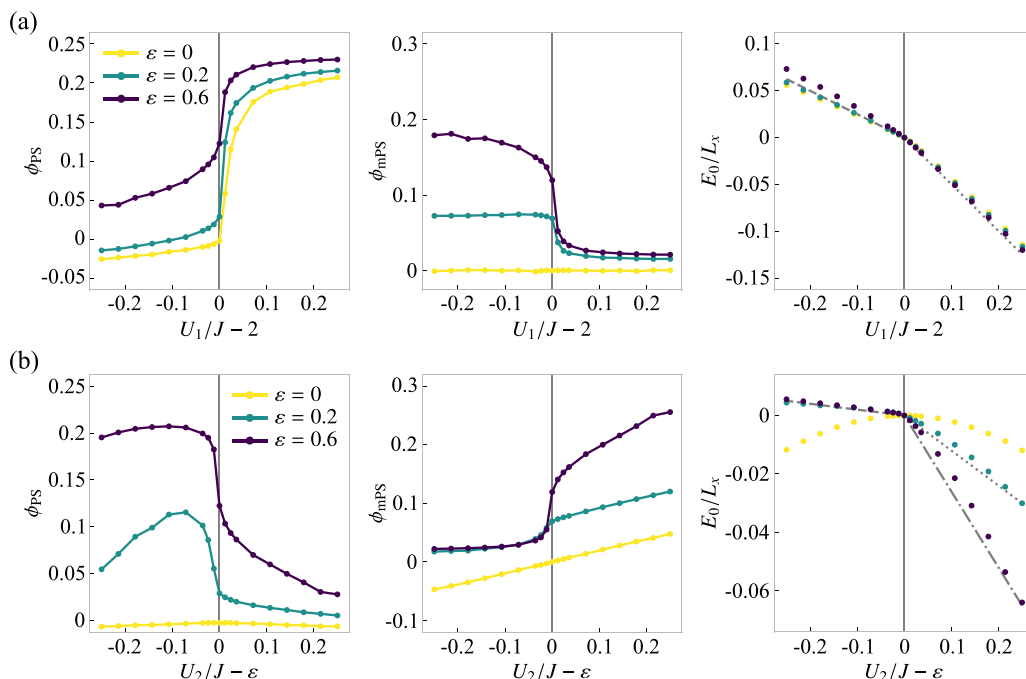


FIG. 23. (a) U_1 dependence with $U_2 = \epsilon J$ and (b) U_2 dependence with $U_1 = 2J$ of ϕ_{PS} , ϕ_{mPS} , and E_0 for $\rho = 0.5$, $h = 0.025J$, and $\epsilon = 0, 0.2$, and 0.6 in 1D systems ($L_x = 100$). The classical condition is indicated with the gray vertical line. For reference, in the figures of E_0 , we also plotted $\langle H \rangle_C$ for (a) the disordered state with no spatial correlation (dashed) and the fPS state (dotted) or (b) the fpmPS states with $N_{\text{cl}} = 1$ (dashed), $N_{\text{cl}} = 6$ (dotted), and $N_{\text{cl}} = 13$ (dash-dotted). We set $\Delta t = 1/[N(2J + h)]$ and took $N_c = 10^4$ and $M = 2 \times 10^5 N$ for (a), while $N_c = 10^5$ and $M = 10^4 N$ for (b).

transition rate matrix and D is a diagonal matrix that represents the deviation from the classical line. Defining $-d$ as the smallest diagonal element of $W + D$, $W + D + dI$ is a non-negative matrix, where I is the identity matrix. According to the Perron-Frobenius theorem, the eigenvalue with the largest real part for $W + D + dI$ (i.e., $-E_0 + d$) is bounded from above as

$$-E_0 + d \leq \max_j \sum_i (W + D + dI)_{ij}. \quad (\text{D5})$$

Since $\sum_i W_{ij} = 0$, $\sum_i D_{ij} = D_{jj}$, and $\sum_i I_{ij} = 1$, we obtain a lower bound of the ground state energy as $E_0 \geq -\max_j D_{jj}$.

4. Energy of different states

For an arbitrary state $|\psi\rangle = \sum_C P(C) |C\rangle$, where $|C\rangle$ is the Fock basis, we can calculate $\langle H \rangle_C$ as

$$\langle H \rangle_C = \sum_C \left[(2J - U_1) \sum_{(i,j)} n_i n_j + (\epsilon J - U_2) \sum_i m_i (n_{i+\hat{x}} - n_{i-\hat{x}}) \right] P(C) / \sum_C P(C). \quad (\text{D6})$$

Here, n_i and m_i are the local density and magnetization for the configuration C , respectively.

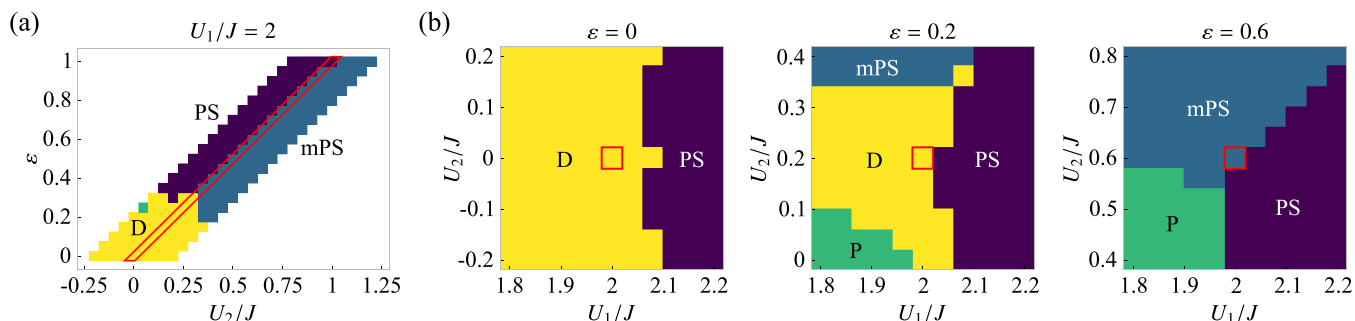


FIG. 24. Ground-state phase diagrams of the 1D quantum model. (a) U_2 - ϵ phase diagram for $U_1 = 2J$ around the classical line (red box) with PS ($\phi_{\text{PS}} > 0.1$ and $\phi_{\text{mPS}} \leq 0.1$), mPS ($\phi_{\text{mPS}} > 0.1$), P (polar, $M^2 > 0.1$), and D (disordered, otherwise) states. (b) U_1 - U_2 phase diagrams for $\epsilon = 0, 0.2, 0.6$ around the cross section of the classical line (red box). In all figures, we set $\rho = 0.5$ and $h = 0.025J$. Simulation parameters are $\Delta t = 1/[N(2J + h)]$, $N_c = 10^4$, and $M = 10^4 N$.

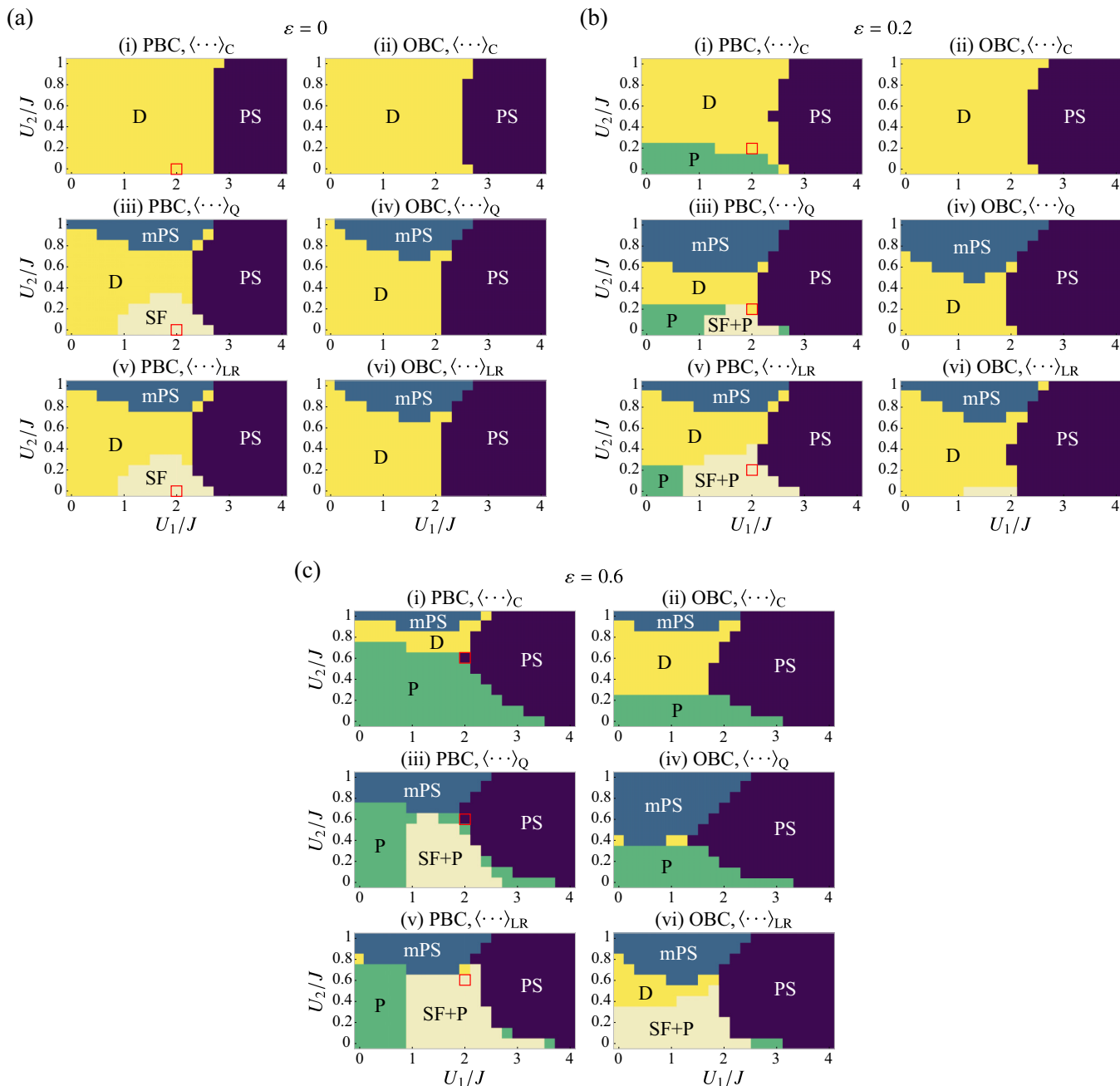


FIG. 25. U_1 - U_2 phase diagrams in small 1D systems. We used $L_x = 12$ and (a) $\varepsilon = 0$, (b) 0.2, and (c) 0.6, with PS ($\phi_{\text{PS}} > 0.05$ and $\phi_{\text{mPS}} \leq 0.3$), mPS ($\phi_{\text{mPS}} > 0.3$), P (polar, $M^2 > 0.2$), SF (superfluid, $\phi_{\text{SF}} > 0.2$), and D (disordered, otherwise) states. The order parameters are calculated by exact diagonalization, using (i, ii) $\langle \cdots \rangle_{\text{C}}$, (iii, iv) $\langle \cdots \rangle_{\text{Q}}$, or (v, vi) $\langle \cdots \rangle_{\text{LR}}$, for the PBC (i, iii, v) or OBC (ii, iv, vi).

In Fig. 6, we plotted $\langle H \rangle_{\text{C}}$ calculated for the disordered state with no spatial correlation, the fully phase-separated (fPS) state, and the fully polarized microphase-separated (fpmPS) state (Fig. 18). First, the disordered state with no spatial correlation is defined as $|\psi\rangle = (\sum_{i,s} a_{i,s}^\dagger)^N |0\rangle$, and the corresponding energy is $\langle H \rangle_{\text{C}} = 2(2J - U_1)\rho^2 L_x L_y$ by neglecting $o(L_x L_y)$, which we plot in Fig. 6(a) (dashed line). Second, we define a fPS state as $|\psi\rangle = \prod_{i \in \Omega} (a_{i,+}^\dagger + a_{i,-}^\dagger) |0\rangle$, where Ω is an area containing N sites and minimizing the circumference [Fig. 18(a)]. The corresponding energy is $\langle H \rangle_{\text{C}} = 2(2J - U_1)\rho L_x L_y$ by neglecting

$o(L_x L_y)$, which we plot in Fig. 6(a) (dotted line). Lastly, we define a fpmPS state with N_{cl} clusters, assuming commensurability, as $|\psi\rangle = \prod_{n=1}^{N_{\text{cl}}} \prod_{i \in \Omega_n \setminus (\partial \Omega_n^L \cup \partial \Omega_n^R)} (a_{i,+}^\dagger + a_{i,-}^\dagger) \prod_{i \in \partial \Omega_n^L} a_{i,+}^\dagger \prod_{i \in \partial \Omega_n^R} a_{i,-}^\dagger |0\rangle$, where Ω_n is the n th rectangular area and $\partial \Omega_n^{L(R)}$ is its left (right) boundary [Fig. 18(b)]. The corresponding energy is $\langle H \rangle_{\text{C}} = (2J - U_1)(2\rho L_x L_y - N_{\text{cl}} L_y) + 2(\varepsilon J - U_2)N_{\text{cl}} L_y$, which we plot with $N_{\text{cl}} = 1$ (dashed line) and with $N_{\text{cl}} = 4$ (dotted line) in Fig. 6(b). Note that, for $U_2 \gg J, h, U_1 (> 0)$, a fpmPS state with $N_{\text{cl}} = \rho L_x / 2$ [Fig. 18(c)] is the ground state within the first-order perturbation of $h/U_2, J/U_2$, and U_1/U_2 .

5. Convergence of simulations and asymmetric-hopping-induced phase separation

In the diffusion Monte Carlo (DMC) simulations, we checked the convergence to the steady state by examining the initial-state dependence of the results and the relaxation of the order parameters and the ground-state energy. As an illustration, we show the U_1 dependence of ϕ_{PS} and ϕ_{mPS} obtained with the fPS initial state, compared with that obtained with the disordered initial state [Fig. 19(a) and also see Fig. 6(a) in the main text]. Apart from statistical errors, we do not see differences due to initial conditions for the case of system size 30×3 , but there is a discrepancy in the case of 50×5 (see also Fig. 21). This is likely due to the number of clones (N_c) being insufficient for the large system size simulation [96]. Further, we show an example of the time dependence of ϕ_{PS} and E_0 evolving from the disordered initial state in the DMC simulations [Fig. 19(b)], which indicates that the steady state is achieved in the final state. Note that, for $U_1 = 2J$ and $U_2 = \varepsilon J$ (classical condition), E_0 is trivially zero according to the probability conservation.

To confirm the validity of our DMC simulation, we also checked the consistency with exact diagonalization of the 1D counterpart of the Hamiltonian (1). As examples, we compare the ε dependence of the ground-state energy and order parameters obtained by DMC simulations and exact diagonalization for $L_x = 12$, varying the number of clones N_c (Fig. 20). The accuracy of the DMC simulation improves as N_c is increased, apart from statistical errors and systematic errors that occur due to the deviation from the classical line ($\varepsilon = 0$ in Fig. 20) being large [see the approximation in Eq. (C2)].

We also show the U_2 dependence of the order parameters for systems with size 30×3 and 50×5 (Fig. 21). We can see that the polar state with finite M^2 is destabilized and instead the PS state with finite ϕ_{PS} dominates broader parameter regions as the system becomes larger, though the dependence on the initial state remains around the phase boundary in the 50×5 system. Thus the PS state may replace the polar state even for $U_2 = 0$ in larger systems, and thus the asymmetric-hopping-induced phase separation can occur as observed in 1D systems [Fig. 7(b) in the main text].

6. 1D model

For the 1D counterpart of the ALG, we show the ρ and ε dependence [Fig. 22(a)] and the size dependence [Fig. 22(b)] of the order parameter of

phase separation, $\phi_{\text{1D}} [:= -\min C(r)]$, where $C(r) [:= L_x^{-1} \sum_i \langle [n(x_i + r) - \rho][n(x_i) - \rho] \rangle]$ is the 1D density correlation function. The data suggest that the macroscopic MIPS is not stable in the thermodynamic limit ($\phi_{\text{1D}} \rightarrow 0$ for $L_x \rightarrow \infty$). This result is consistent with preceding studies of similar 1D models [31,33,97], where the macroscopic MIPS does not occur due to the spontaneous formation of domain boundaries.

For the quantum model, Figs. 23 and 24 show the 1D counterparts of Figs. 6 and 8 in the main text, respectively. We can see that the discontinuous transition occurs in crossing the classical line (Fig. 23) as observed in 2D systems, and the topology of the phase diagrams (Fig. 24) is also similar. Note that in 1D systems with finite ε or U_2 , the mPS order parameter $\phi_{\text{mPS}} [:= L_x^{-1} \sum_{i=1}^{L_x} \langle \hat{n}_i(\hat{n}_{i+1} - \hat{n}_{i-1}) \rangle_C]$ is generically nonzero even for $L_x \rightarrow \infty$, and consequently the disordered and mPS states are indistinguishable from the symmetry perspective.

APPENDIX E: QUANTUM PHASE DIAGRAMS IN SMALL 1D SYSTEMS

To clarify how the phase diagrams depend on the definition of order parameters and the boundary condition, we calculated the order parameters using exact diagonalization in small 1D systems. On top of the expectation values defined in the main text, we consider $\langle \cdots \rangle_{\text{LR}} = \langle \psi'_0 | \cdots | \psi_0 \rangle$ with $\langle \psi'_0 |$ being the left ground state. We additionally define the order parameters, ϕ_{PS} , ϕ_{mPS} , M^2 , and ϕ_{SF} for $\langle \cdots \rangle_{\text{LR}}$.

The results are summarized in the phase diagrams (Fig. 25). First, we find that all the states predicted using $\langle \cdots \rangle_C$ with the PBC [(i) in Figs. 25(a)–25(c)] appear, regardless of the definition of order parameters or the boundary condition. Thus the DMC simulation, which is applicable to larger systems as demonstrated in the main text, is useful in qualitatively predicting the phase diagram (apart from the SF order) in the experimentally relevant case, where we use $\langle \cdots \rangle_Q$ with the OBC. Next, focusing on the cases with the PBC, we see that the SF state appears for $\varepsilon = 0$ [(iii, v) in Fig. 25(a)] consistently with the previous studies of the Hermitian hard-core boson models [72]. Interestingly, the SF state with polar order is stable for finite ε [(iii, v) in Figs. 25(b) and 25(c)]. Lastly, since the OBC prevents the particles from flowing, the polar order is suppressed [(ii, iv, vi) in Fig. 25(b)] unless ε is large enough [(ii, iv, vi) in Fig. 25(c)].

[1] M. C. Marchetti, J. F. Joanny, S. Ramaswamy, T. B. Liverpool, J. Prost, M. Rao, and R. A. Simha, Hydrodynamics of soft active matter, *Rev. Mod. Phys.* **85**, 1143 (2013).
 [2] L. M. Nash, D. Kleckner, A. Read, V. Vitelli, A. M. Turner, and W. T. Irvine, Topological mechanics of gyroscopic metamaterials, *Proc. Natl Acad. Sci. USA* **112**, 14495 (2015).
 [3] D. Banerjee, A. Souslov, A. G. Abanov, and V. Vitelli, Odd viscosity in chiral active fluids, *Nat. Commun.* **8**, 1 (2017).
 [4] T. Sanchez, D. T. Chen, S. J. DeCamp, M. Heymann, and Z. Dogic, Spontaneous motion in hierarchically

assembled active matter, *Nature (London)* **491**, 431 (2012).

[5] K. Kawaguchi, R. Kageyama, and M. Sano, Topological defects control collective dynamics in neural progenitor cell cultures, *Nature (London)* **545**, 327 (2017).
 [6] J. Prost, F. Jülicher, and J.-F. Joanny, Active gel physics, *Nat. Phys.* **11**, 111 (2015).
 [7] D. Needleman and Z. Dogic, Active matter at the interface between materials science and cell biology, *Nat. Rev. Mater.* **2**, 17048 (2017).

- [8] G. Gompper, R. G. Winkler, T. Speck, A. Solon, C. Nardini, F. Peruani, H. Löwen, R. Golestanian, U. B. Kaupp, L. Alvarez, T. Kiørboe, E. Lauga, W. C. K. Poon, A. DeSimone, S. Muiños-Landin, A. Fischer, N. A. Söker, F. Cichos, R. Kapral, P. Gaspard, M. Ripoll, F. Sagues, A. Doostmohammadi, J. M. Yeomans, I. S. Aranson, C. Bechinger, H. Stark, C. K. Hemelrijk, F. J. Nedelec, T. Sarkar, T. Aryaksama, M. Lacroix, G. Duclos, V. Yashunsky, P. Silberzan, M. Arroyo, and S. Kale, The 2020 motile active matter roadmap, *J. Phys.: Condens. Matter* **32**, 193001 (2020).
- [9] J. Toner and Y. Tu, Flocks, herds, and schools: A quantitative theory of flocking, *Phys. Rev. E* **58**, 4828 (1998).
- [10] J. Alicea, L. Balents, M. P. A. Fisher, A. Paramekanti, and L. Radzihovsky, Transition to zero resistance in a two-dimensional electron gas driven with microwaves, *Phys. Rev. B* **71**, 235322 (2005).
- [11] A. Mitra, S. Takei, Y. B. Kim, and A. J. Millis, Nonequilibrium Quantum Criticality in Open Electronic Systems, *Phys. Rev. Lett.* **97**, 236808 (2006).
- [12] S. Takei and Y. B. Kim, Nonequilibrium-induced metal-superconductor quantum phase transition in graphene, *Phys. Rev. B* **78**, 165401 (2008).
- [13] B. Loewe, A. Souslov, and P. M. Goldbart, Flocking from a quantum analogy: Spin-orbit coupling in an active fluid, *New J. Phys.* **20**, 013020 (2018).
- [14] M. Müller, S. Diehl, G. Pupillo, and P. Zoller, Engineered open systems and quantum simulations with atoms and ions, *Adv. At. Mol. Opt. Phys.* **61**, 1 (2012).
- [15] A. J. Daley, Quantum trajectories and open many-body quantum systems, *Adv. Phys.* **63**, 77 (2014).
- [16] F. Schäfer, T. Fukuhara, S. Sugawa, Y. Takasu, and Y. Takahashi, Tools for quantum simulation with ultracold atoms in optical lattices, *Nat. Rev. Phys.* **2**, 411 (2020).
- [17] Y. Ashida, Z. Gong, and M. Ueda, Non-hermitian physics, *Adv. Phys.* **69**, 249 (2020).
- [18] Y. C. Hu and T. L. Hughes, Absence of topological insulator phases in non-hermitian pt -symmetric hamiltonians, *Phys. Rev. B* **84**, 153101 (2011).
- [19] K. Esaki, M. Sato, K. Hasebe, and M. Kohmoto, Edge states and topological phases in non-hermitian systems, *Phys. Rev. B* **84**, 205128 (2011).
- [20] H. Shen, B. Zhen, and L. Fu, Topological Band Theory for Non-Hermitian Hamiltonians, *Phys. Rev. Lett.* **120**, 146402 (2018).
- [21] Z. Gong, Y. Ashida, K. Kawabata, K. Takasan, S. Higashikawa, and M. Ueda, Topological Phases of Non-Hermitian Systems, *Phys. Rev. X* **8**, 031079 (2018).
- [22] S. Yao and Z. Wang, Edge States and Topological Invariants of Non-Hermitian Systems, *Phys. Rev. Lett.* **121**, 086803 (2018).
- [23] K. Kawabata, K. Shiozaki, M. Ueda, and M. Sato, Symmetry and Topology in Non-Hermitian Physics, *Phys. Rev. X* **9**, 041015 (2019).
- [24] T. Ozawa, H. M. Price, A. Amo, N. Goldman, M. Hafezi, L. Lu, M. C. Rechtsman, D. Schuster, J. Simon, O. Zilberberg, and I. Carusotto, Topological photonics, *Rev. Mod. Phys.* **91**, 015006 (2019).
- [25] L. Li, C. H. Lee, S. Mu, and J. Gong, Critical non-hermitian skin effect, *Nat. Commun.* **11**, 5491 (2020).
- [26] Y. Ashida, S. Furukawa, and M. Ueda, Parity-time-symmetric quantum critical phenomena, *Nat. Commun.* **8**, 15791 (2017).
- [27] M. Nakagawa, N. Kawakami, and M. Ueda, Non-Hermitian Kondo Effect in Ultracold Alkaline-Earth Atoms, *Phys. Rev. Lett.* **121**, 203001 (2018).
- [28] R. Hamazaki, K. Kawabata, and M. Ueda, Non-Hermitian Many-Body Localization, *Phys. Rev. Lett.* **123**, 090603 (2019).
- [29] K. Kawabata and S. Ryu, Nonunitary Scaling Theory of Non-Hermitian Localization, *Phys. Rev. Lett.* **126**, 166801 (2021).
- [30] M. Kourbane-Houssene, C. Erignoux, T. Bodineau, and J. Tailleur, Exact Hydrodynamic Description of Active Lattice Gases, *Phys. Rev. Lett.* **120**, 268003 (2018).
- [31] M. E. Cates and J. Tailleur, Motility-induced phase separation, *Ann. Rev. Condens. Matter Phys.* **6**, 219 (2015).
- [32] Y. Fily and M. C. Marchetti, Athermal Phase Separation of Self-Propelled Particles with no Alignment, *Phys. Rev. Lett.* **108**, 235702 (2012).
- [33] A. G. Thompson, J. Tailleur, M. E. Cates, and R. A. Blythe, Lattice models of nonequilibrium bacterial dynamics, *J. Stat. Mech.* (2011) P02029.
- [34] I. Buttinoni, J. Bialké, F. Kümmel, H. Löwen, C. Bechinger, and T. Speck, Dynamical Clustering and Phase Separation in Suspensions of Self-Propelled Colloidal Particles, *Phys. Rev. Lett.* **110**, 238301 (2013).
- [35] G. Liu, A. Patch, F. Bahar, D. Yllanes, R. D. Welch, M. C. Marchetti, S. Thutupalli, and J. W. Shaevitz, Self-Driven Phase Transitions Drive Myxococcus Xanthus Fruiting Body Formation, *Phys. Rev. Lett.* **122**, 248102 (2019).
- [36] A. P. Solon, J. Stenhammar, M. E. Cates, Y. Kafri, and J. Tailleur, Generalized thermodynamics of phase equilibria in scalar active matter, *Phys. Rev. E* **97**, 020602(R) (2018).
- [37] A. P. Solon, J. Stenhammar, M. E. Cates, Y. Kafri, and J. Tailleur, Generalized thermodynamics of motility-induced phase separation: phase equilibria, laplace pressure, and change of ensembles, *New J. Phys.* **20**, 075001 (2018).
- [38] J. T. Siebert, F. Dittrich, F. Schmid, K. Binder, T. Speck, and P. Virnau, Critical behavior of active brownian particles, *Phys. Rev. E* **98**, 030601(R) (2018).
- [39] B. Partridge and C. F. Lee, Critical Motility-Induced Phase Separation Belongs to the Ising Universality Class, *Phys. Rev. Lett.* **123**, 068002 (2019).
- [40] C. Maggi, M. Paoluzzi, A. Crisanti, E. Zaccarelli, and N. Gnan, Universality class of the motility-induced critical point in large scale off-lattice simulations of active particles, *Soft Matter* **17**, 3807 (2021).
- [41] F. Dittrich, T. Speck, and P. Virnau, Critical behaviour in active lattice models of motility-induced phase separation, *Eur. Phys. J. E* **44**, 53 (2021).
- [42] E. Tjhung, C. Nardini, and M. E. Cates, Cluster Phases and Bubbly Phase Separation in Active Fluids: Reversal of the Ostwald Process, *Phys. Rev. X* **8**, 031080 (2018).
- [43] F. Caballero, C. Nardini, and M. E. Cates, From bulk to microphase separation in scalar active matter: a perturbative renormalization group analysis, *J. Stat. Mech.* (2018) 123208.
- [44] X.-Q. Shi, G. Fausti, H. Chaté, C. Nardini, and A. Solon, Self-Organized Critical Coexistence Phase in Repulsive Active Particles, *Phys. Rev. Lett.* **125**, 168001 (2020).
- [45] B. Schmittmann and R. Zia, *Statistical Mechanics of Driven Diffusive System*, edited by C. Domb and J. Lebowitz, Phase Transitions and Critical Phenomena (Academic Press, New York, 1995), Vol. 17.

- [46] J. Marro and R. Dickman, *Nonequilibrium Phase Transitions in Lattice Models*, Collection alea-saclay: Monographs and texts in statistical physics (Cambridge University Press, Cambridge, 1999).
- [47] B. Schmittmann and R. Zia, Driven diffusive systems. an introduction and recent developments, *Phys. Rep.* **301**, 45 (1998).
- [48] R. K. P. Zia, Twenty five years after kls: A celebration of non-equilibrium statistical mechanics, *J. Stat. Phys.* **138**, 20 (2010).
- [49] A. P. Solon and J. Tailleur, Revisiting the Flocking Transition Using Active Spins, *Phys. Rev. Lett.* **111**, 078101 (2013).
- [50] A. P. Solon and J. Tailleur, Flocking with discrete symmetry: The two-dimensional active ising model, *Phys. Rev. E* **92**, 042119 (2015).
- [51] T. Vicsek and A. Zafeiris, Collective motion, *Phys. Rep.* **517**, 71 (2012).
- [52] M. Doi, Second quantization representation for classical many-particle system, *J. Phys. A* **9**, 1465 (1976).
- [53] L. Peliti, Path integral approach to birth-death processes on a lattice, *J. Phys. France* **46**, 1469 (1985).
- [54] B. Schmittmann, K. Hwang, and R. K. P. Zia, Onset of spatial structures in biased diffusion of two species, *Europhys. Lett.* **19**, 19 (1992).
- [55] K. E. Bassler, B. Schmittmann, and R. K. P. Zia, Spatial structures with non-zero winding number in biased diffusion of two species, *Europhys. Lett.* **24**, 115 (1993).
- [56] D. P. Foster and C. Godrèche, Finite-size effects for phase segregation in a two-dimensional asymmetric exclusion model with two species, *J. Stat. Phys.* **76**, 1129 (1994).
- [57] G. Korniss, B. Schmittmann, and R. K. P. Zia, Nonequilibrium phase transitions in a simple three-state lattice gas, *J. Stat. Phys.* **86**, 721 (1997).
- [58] K.-T. Leung, Finite-Size Scaling of Driven Diffusive Systems: Theory and Monte Carlo Studies, *Phys. Rev. Lett.* **66**, 453 (1991).
- [59] J.-S. Wang, Anisotropic finite-size scaling analysis of a two-dimensional driven diffusive system, *J. Stat. Phys.* **82**, 1409 (1996).
- [60] A. Lefèvre and G. Biroli, Dynamics of interacting particle systems: stochastic process and field theory, *J. Stat. Mech.* (2007) P07024.
- [61] P. C. Martin, E. D. Siggia, and H. A. Rose, Statistical dynamics of classical systems, *Phys. Rev. A* **8**, 423 (1973).
- [62] H.-K. Janssen, On a lagrangean for classical field dynamics and renormalization group calculations of dynamical critical properties, *Z. Phys. B* **23**, 377 (1976).
- [63] C. De Dominicis, Techniques de renormalisation de la théorie des champs et dynamique des phénomènes critiques, *J. Phys. Colloq.* **37**, C1 (1976).
- [64] V. Démery, O. Bénichou, and H. Jacquin, Generalized langevin equations for a driven tracer in dense soft colloids: construction and applications, *New J. Phys.* **16**, 053032 (2014).
- [65] A. Poncet, O. Bénichou, V. Démery, and G. Oshanin, Universal Long Ranged Correlations in Driven Binary Mixtures, *Phys. Rev. Lett.* **118**, 118002 (2017).
- [66] A. Poncet, O. Bénichou, V. Démery, and D. Nishiguchi, Pair correlation of dilute active brownian particles: From low-activity dipolar correction to high-activity algebraic depletion wings, *Phys. Rev. E* **103**, 012605 (2021).
- [67] C. Yeung, T. Rogers, A. Hernandez-Machado, and D. Jasnow, Phase separation dynamics in driven diffusive systems, *J. Stat. Phys.* **66**, 1071 (1992).
- [68] B. Schmittmann and R. K. P. Zia, Critical Properties of a Randomly Driven Diffusive System, *Phys. Rev. Lett.* **66**, 357 (1991).
- [69] B. Schmittmann, Fixed-point hamiltonian for a randomly driven diffusive system, *Europhys. Lett.* **24**, 109 (1993).
- [70] E. L. Praestgaard, H. Larsen, and R. K. P. Zia, Finite-size scaling in a two-temperature lattice gas: A Monte Carlo study of critical properties, *Europhys. Lett.* **25**, 447 (1994).
- [71] E. L. Præstgaard, B. Schmittmann, and R. K. P. Zia, A lattice gas coupled to two thermal reservoirs: Monte Carlo and field theoretic studies, *Eur. Phys. J. B* **18**, 675 (2000).
- [72] T. Matsubara and H. Matsuda, A lattice model of liquid helium, I, *Prog. Theor. Phys.* **16**, 569 (1956).
- [73] O. S. Sariyer, Two-dimensional quantum-spin-1/2 XXZ magnet in zero magnetic field: Global thermodynamics from renormalisation group theory, *Philos. Mag.* **99**, 1787 (2019).
- [74] C. Giardinà, J. Kurchan, and L. Peliti, Direct Evaluation of Large-Deviation Functions, *Phys. Rev. Lett.* **96**, 120603 (2006).
- [75] T. Vicsek, A. Czirók, E. Ben-Jacob, I. Cohen, and O. Shochet, Novel Type of Phase Transition in A System of Self-Driven Particles, *Phys. Rev. Lett.* **75**, 1226 (1995).
- [76] J. L. Lebowitz and H. Spohn, A Gallavotti–Cohen-type symmetry in the large deviation functional for stochastic dynamics, *J. Stat. Phys.* **95**, 333 (1999).
- [77] J. P. Garrahan, R. L. Jack, V. Lecomte, E. Pitard, K. van Duijvendijk, and F. van Wijland, Dynamical First-Order Phase Transition in Kinetically Constrained Models of Glasses, *Phys. Rev. Lett.* **98**, 195702 (2007).
- [78] S. Whitelam, K. Klymko, and D. Mandal, Phase separation and large deviations of lattice active matter, *J. Chem. Phys.* **148**, 154902 (2018).
- [79] T. Nemoto, E. Fodor, M. E. Cates, R. L. Jack, and J. Tailleur, Optimizing active work: Dynamical phase transitions, collective motion, and jamming, *Phys. Rev. E* **99**, 022605 (2019).
- [80] L. Tociu, E. Fodor, T. Nemoto, and S. Vaikuntanathan, How Dissipation Constrains Fluctuations in Nonequilibrium Liquids: Diffusion, Structure, and Biased Interactions, *Phys. Rev. X* **9**, 041026 (2019).
- [81] J. P. Garrahan, R. L. Jack, V. Lecomte, E. Pitard, K. van Duijvendijk, and F. van Wijland, First-order dynamical phase transition in models of glasses: An approach based on ensembles of histories, *J. Phys. A* **42**, 075007 (2009).
- [82] W. S. Bakr, A. Peng, M. E. Tai, R. Ma, J. Simon, J. I. Gillen, S. Fölling, L. Pollet, and M. Greiner, Probing the superfluid–to–mott insulator transition at the single-atom level, *Science* **329**, 547 (2010).
- [83] C. Gross and I. Bloch, Quantum simulations with ultracold atoms in optical lattices, *Science* **357**, 995 (2017).
- [84] J. Dalibard, Y. Castin, and K. Mølmer, Wave-Function Approach to Dissipative Processes in Quantum Optics, *Phys. Rev. Lett.* **68**, 580 (1992).
- [85] R. Dum, P. Zoller, and H. Ritsch, Monte Carlo simulation of the atomic master equation for spontaneous emission, *Phys. Rev. A* **45**, 4879 (1992).
- [86] H. Carmichael, *An Open Systems Approach to Quantum Optics* (Springer, Berlin, 1993).

- [87] R. Landig, L. Hruby, N. Dogra, M. Landini, R. Mottl, T. Donner, and T. Esslinger, Quantum phases from competing short- and long-range interactions in an optical lattice, *Nature (London)* **532**, 476 (2016).
- [88] A. Browaeys and T. Lahaye, Many-body physics with individually controlled Rydberg atoms, *Nat. Phys.* **16**, 132 (2020).
- [89] C. Trefzger, C. Menotti, B. Capogrosso-Sansone, and M. Lewenstein, Ultracold dipolar gases in optical lattices, *J. Phys. B* **44**, 193001 (2011).
- [90] H. Zhao, J. Knolle, and F. Mintert, Engineered nearest-neighbor interactions with doubly modulated optical lattices, *Phys. Rev. A* **100**, 053610 (2019).
- [91] K. Yamamoto, M. Nakagawa, K. Adachi, K. Takasan, M. Ueda, and N. Kawakami, Theory of Non-Hermitian Fermionic Superfluidity with a Complex-Valued Interaction, *Phys. Rev. Lett.* **123**, 123601 (2019).
- [92] H. Wang, L.-J. Lang, and Y. D. Chong, Non-hermitian dynamics of slowly varying hamiltonians, *Phys. Rev. A* **98**, 012119 (2018).
- [93] A. Murugan and S. Vaikuntanathan, Topologically protected modes in non-equilibrium stochastic systems, *Nat. Commun.* **8**, 13881 (2017).
- [94] L. Martino, V. Elvira, and F. Louzada, Effective sample size for importance sampling based on discrepancy measures, *Signal Process.* **131**, 386 (2017).
- [95] N. Cerf and O. C. Martin, Finite population-size effects in projection Monte Carlo methods, *Phys. Rev. E* **51**, 3679 (1995).
- [96] T. Nemoto, F. Bouchet, R. L. Jack, and V. Lecomte, Population-dynamics method with a multicanonical feedback control, *Phys. Rev. E* **93**, 062123 (2016).
- [97] R. Soto and R. Golestanian, Run-and-tumble dynamics in a crowded environment: Persistent exclusion process for swimmers, *Phys. Rev. E* **89**, 012706 (2014).